Field measurements, laboratory tests and empirical relations for investigating the solid-to-fluid transition of a rapid earthflow

Published Version:
Field measurements, laboratory tests and empirical relations for investigating the solid-to-fluid transition of a rapid earthflow / Berti M.; Castellaro S.; Zuccarini A.. - In: ENGINEERING GEOLOGY. - ISSN 0013-7952. - STAMPA. - 296:(2022), pp. 106486.1-106486.13. [10.1016/j.enggeo.2021.106486]

Availability:
This version is available at: https://hdl.handle.net/11585/870220 since: 2022-02-26

Published:
DOI: http://doi.org/10.1016/j.enggeo.2021.106486

(Article begins on next page)

Dynamics of an active earthflow inferred from surface-wave monitoring

Lara Bertello[1], Matteo Berti[1], Silvia Castellaro[2], Gabriela Squarzoni[1]

[1] Department of Biological, Geological and Environmental Sciences, University of Bologna, 40127, Bologna, Italy

[2] Department of Physics and Astronomy, University of Bologna, 40127, Bologna, Italy

Corresponding author:

- Matteo Berti matteo.berti@unibo.it

Key Points:

- The earthflow material at our study site undergoes significant changes in shear stiffness during rapid movements
- Rayleigh velocity decreases as the earthflow accelerates, then gradually increases through time as the landslide decelerates
- Internal deformation clearly played an important role in the dynamics of the Montevecchio earthflow

Abstract

Earthflows are clay-rich, slow-moving landslides subjected to periodic accelerations. During the stage of rapid movement, most earthflows exhibit a change in behavior from a solid to a fluid-like state. Although this behavior has been extensively documented in the field, the mechanism leading to the rapid acceleration of earthflows is still poorly understood. Some studies suggest that earthflows essentially behave as Coulomb plastic solids, attributing the flow-like appearance to distributed internal shearing; others believe that these landslides can be treated as viscous fluids, pointing out that the material undergoes a phase transition by increasing its moisture content. Minimal data are currently available to support these different findings. In this study, we present the results of periodic and continuous measurements of Rayleigh wave velocity carried out in an active earthflow located in the Northern Apennines of Italy. Our data indicate that the material undergoes significant changes in shear stiffness and undrained strength during rapid movements. In particular, the material exhibits a substantial drop of Rayleigh wave velocity as the earthflow accelerates, followed by a slow return to pre-disturbance Rayleigh velocities as the landslide decelerates. Soon after a surge, the earthflow material is extremely soft and the estimated gravimetric water content is above the liquid limit. In the following months, the shear stiffness gradually increases and the water content decreases to the plastic limit following a non-linear trend typical of a consolidation process. These data demonstrate that the earthflow transforms into a viscous fluid by softening of the material and by water entrainment.

1 Introduction

Earthflows are among the most common type of landslides in many mountainous areas [*Keefer and Johnson,* 1983*; Hungr et al.,* 2001*; Picarelli et al.,* 2005; *Simoni et al.*, 2013]. They occur in fine-grained materials and are identified by a tongue or teardrop shape elongated in the downslope direction [*Hutchinson,* 1988*; Cruden and Varnes,* 1996]. A specific feature of these landslides is their complex style of movement [*Hutchinson,* 1970*; Bovis and Jones,* 1992]. Earthflows can continue to move slowly at a rate of less than 1 m per year over a long a period, primarily by sliding on discrete basal and lateral slip surfaces [*Keefer and Johnson,* 1983*; Baum et al.,* 2003*; Schulz et al.,* 2009]. Then, in response to critical rainfall conditions, they may suddenly accelerate and attain high velocities (up to several m/h) for a limited time [*Varnes and Savage,* 1996*; Coe et al.,* 2009]. During the surge of rapid movement, most earthflows create geomorphic features like bulging toes, arcuate ridges, and streamlines that suggest a flow-like behavior [*D'Elia et al,* 1998*; Giordan et al.,* 2013*; Handwerger et al.,* 2013].

Many researchers believe that the ability of earthflows to surge and rapidly accelerate is a consequence of excess pore-water pressures generated along shear surfaces [*Keefer and Johnson,* 1983*; Baum et al.,* 2003*; van Asch and Malet*, 2009]. Others point out that such a behavior indicates a sudden change in the mechanical properties of the material, like a loss of shear stiffness or an increase of water content [*Picarelli et al.,* 2005*; Pastor et al.,* 2009*; Pastor et al.,* 2010*; Jongmans et al.,* 2015]. Although these factors are not mutually exclusive (an earthflow could be triggered by an increase of pore-water pressures and subsequently undergo a change in mechanical properties as the movement continues) their relative importance is still poorly understood.

Pore-water pressure is certainly the most significant factor that can trigger the initial movement, increase the displacement rate, or move earthflows on very gentle slopes [*Hutchinson and Bhandari,* 1971*; Iverson and Major,* 1987*; Coe et al.,* 2009]. However, clay-rich soils do not liquefy under an increase of pore water pressure [e.g. *Seed et al.,* 2003]. In soil mechanics, the term "liquefaction" denotes a condition where a granular material behaves like a fluid because the effective interparticle stress σ' (given by the difference between the total overburden stress σ and the pore-water pressure u; *Terzaghi,* 1943) reduces essentially to zero causing the particles to lose contact with each other. Soil liquefaction occurs in loosely packed, cohesionless soils (mostly sand) that tend to decrease in volume when subjected to shear stress [*Seed et al.,* 2003]. Clay materials with measurable plasticity are not susceptible to liquefaction because they have undrained cohesion, thus the shear strength of clays does not become zero when the effective stress becomes zero [*Seed et al.,* 2003*; Robertson,* 2010]. Accordingly, most researchers consider earthflows as Coulomb plastic solids that primarily move by sliding, and attribute the flow-like appearance to distributed internal shearing rather than mass liquefaction [*Keefer and Johnson* 1983; *Baum et al.,* 2003*; Hungr et al.,* 2001].

Nevertheless, fine-grained materials can change from solid to plastic to fluid as the water content increases, showing distinct changes in behavior and consistency. The Atterberg limits are a conventional measure of the critical water contents at which these changes occur [*Casagrande,* 1932]. The transition from a plastic to a fluid state due to an increase of the water content is referred to hereafter as "fluidization". Fluidization differs from liquefaction because the material undergoes a change in behavior with a change in volume, while liquefaction essentially assumes undrained conditions and constant void ratio. Field observations indicate that earthflows may exhibit a significant increase in water content during mobilization [*Prior et al.,* 1968*; Hutchinson et al.,* 1974]. Most active earthflows are so soft that they do not support a person's weight [*Keefer and Johnson* 1983], or become "so wet and mascerated that all the debris may truly flow by continuous internal deformation" [*Craig* 1979 cited in *Moore* 1988, p. 59]. Fluid rheologists have extensively investigated the solid-fluid transition of clays in laboratory rheometrical tests, defining the existence of a yield stress that separates a rigid/elastic domain and a fluid domain [*Coussot et al.,* 1998*; Ancey,* 2007*; Mainsant et al.,* 2012b]. Most of these experiments are conducted on clay slurries at or above the liquid limit (LL), which is the moisture content at which soil changes from a plastic to a fluid state measured using the conventional Casagrande apparatus [*Casagrande*, 1932].

The reasons for this different behavior (shear sliding of a plastic solid vs viscous flow of a liquid material) are still unclear, but more can be learned by collecting relevant data from rapidly moving earthflows. The monitoring technique recently proposed by *Mainsant et al.* [2012a] can be useful for this purpose. The method relies on the continuous measurement of Rayleigh wave velocity (V_R) as an indicator of material fluidization (or loss of stiffness). Rayleigh waves are elastic waves which travel near the ground surface with a combination of longitudinal compression and dilation [*Richart et al.,* 1970]. These waves are the principal component of ground roll and propagate about 10% slower than shear waves [*Telford et al.,* 1990]. The idea behind the method is that, as the shear wave velocity in a fluid tends to zero [*Reynolds,* 1997], the Rayleigh wave velocity measured inside a landslide should strongly decrease if the solid material fluidizes [*Mainsant et al.,* 2012a*, Mainsant et al.,* 2015]. *Mainsant et al.* [2012a] monitored an earthflow located in the Swiss Alps and observed that Rayleigh velocities decreased continuously and rapidly for several days before a catastrophic stage of movement, suggesting a dramatic change in the mechanical properties of the material. To our knowledge, this is the only study that has documented the process of solid-to-fluid transition in earthflows. Therefore, more field data need to be collected in different geological and morphological settings in order to understand if rapid surging of earthflows is accompanied by softening and fluidization of the material, or mainly occurs by shearing along internal and boundary shear surfaces.

In this study, we used Rayleigh wave velocity to investigate the behavior of the Montevecchio landslide, an active earthflow located in the Northern Apennines of Italy (Savio River valley, Province of Cesena). In February 2014, the earthflow entered a period of intense activity that lasted for 17 months until June 2015. During this period, the earthflow experienced three surges of rapid movement characterized by the fluidization of the moving mass. We documented this process by periodic and continuous measurements of Rayleigh wave velocities carried out using the active Multichannel Analysis of Surface Waves (MASW) [*Park et al.,* 1999] and the passive Refraction Microtremors (ReMi) techniques [*Louie,* 2001]. Geophysical data were integrated by continuous measurements of rainfall and landslide displacement. The data reveal a complex relationship between rainfall, displacement rate, and Rayleigh velocity, providing new insight into the dynamics of active earthflows.

2 Study Area

The Montevecchio landslide is located in the Northern Apennines of Italy, approximately 16 km to the south of the city of Cesena. The landslide occupies the valley of the Ribianco Creek, a tributary of the Savio River (Figure 1). The area is characterized by relative gentle slopes (inclination in the range of 7° to 17°) covered by grass and native brush, and ranges in elevation from 70 to 215 m a.s.l.. The upper part of the basin has typical badland morphologies characterized by small gullies, steep slopes (35° to 45°) and low vegetation coverage.

Bedrock geology consists of shallow marine deposits belonging to the Colombacci Formation [*Ricci Lucchi et al.,* 2002]. This Formation was deposited from the Late Miocene to the Holocene with a maximum thickness of 450 meters. In the study area, the Colombacci Formation consists of predominant marly and silty clay interbedded with thin layers of fine sandstone

(sandstone/clay ratio is lower than 1/3). The clay is stiff to very stiff with a dark grey-blue color when fresh, and becomes soft and brown when weathered. The sandstone layers are loose or only weakly cemented, the color turning from grey to yellow with weathering. The Colombacci Formation is well exposed on the source areas of the earthflow (zone A-B-C; Figure 1).

Old landslide deposits originated by multiple earthflow events occupy about 45% percent of the Ribianco basin (Figure 1). These deposits consist of a clay-rich colluvium containing scattered blocks of weakly cemented sandstone of variable size. The slopes covered by landslide deposits have an average inclination of about 13°. These landslides are subjected to periodic reactivations. The term reactivation (or remobilization) is current to indicate a phase of high activity after a long period of dormancy [*Cruden and Varnes,* 1996]. Herein, reactivation is used to indicate a stage of rapid movement (with a velocity of several meters per day or per hour) that leads to the complete mobilization of the earthflow material. In the last 50 years, the Montevecchio landslide reactivated once in 1979, when it almost reached the houses and the road at the toe, then in 1997, 1999, 2002, 2005, 2006, and 2008 with local movements in the upper part of the slope. During the last period of activity (February 2014 to June 2015) the earthflow underwent a new complete remobilization (see next section).

Results from geotechnical tests show that the earthflow material is fairly uniform. It has medium plasticity (Liquid Limit=50%; Plastic Index=26%) and it is composed on average by 15% sand, 45% silt, and 40% clay. Blue methylene tests provide a specific surface of the clay of 112±1 m^2/g, which is a typical value for an illite [*Hang et al.,* 1970] and an activity index of the clay fraction [Acb; *Lautrin,* 1989] equal to 12.5±0.5. The density is 1850 kg/m^3 in saturated conditions and 1500 kg/m^3 for the dry soil (average values of 500 g undisturbed samples taken within one meter of the surface). Direct shear tests give a critical state friction angle ϕ'_{cs}=20° and a residual friction angle ϕ'_r=13°.The local climate is Mediterranean with two main rainy periods from autumn to early winter (October to December) and during spring (March to May). The average annual precipitation is 780 mm and the average annual snowfall is about 30 cm. The average annual temperature is 14°C and it ranges between 17° and 29° during the dry season and between 1° and 20° C during the wet season.

3 Recent activity of the Montevecchio landslide

In February 2014, after a prolonged rainfall of 109 mm in 16 days, the Montevecchio earthflow entered into a new period of activity. The trigger rainfall was above the probabilistic rainfall threshold established for the area [*Berti et al.,* 2012] and caused a large number of landslides in all the Emilia Romagna Region. The activity lasted for 17 months (until June 2015) and within this period the earthflow underwent three major reactivations (1st reactivation: February 1, 2014; 2nd reactivation: February 25, 2015; 3rd reactivation: May 25, 2015). As mentioned above, the term "reactivation" indicates the complete remobilization of the existing landslide deposits from the source area to the toe. Hereafter we also use the term "partial reactivation" to indicate the remobilization of only a portion of the landslide (generally the upper part) and "suspended phase" to indicate the time after a reactivation when the landslide slows down [*Schadler,* 2010]. A reactivation corresponds to a stage of rapid earthflow movement with downslope velocity on the order of meters per hour. This stage generally lasts 2-5 days, then the velocity gradually decreases with time approaching some nonzero value. In fact, during the 17 months of activity, the landslide never stopped and the minimum-recorded velocity was on the order of few mm/day.

The first reactivation (February 1, 2014) started as sliding failure in the source area A (Figure 2a) and caused a retrogression of the headscarp of about 8 m. The landslide quickly propagated downslope (Figure 2b) at a speed of several meters per hour, and in a couple of days reached the toe (Figure 2c-d). Local authorities decided to protect the houses and the road by removing the advancing toe material, which was continuously excavated for weeks and deposited on the fluvial terrace to the other side of the road. In March and April 2014, the earthflow partially reactivated several times after heavy rain. The excavations at the toe continued and four earth berms were built across the landslide to stop the movement (Figure 1). From May 2014, the earthflow entered a suspended phase that lasted about 9 months. During this period, the landslide velocity decreased gradually from m/day to cm/day, with episodes of acceleration of 10-20 cm in a few days after intense rainfall events. The suspend phase ended with the second reactivation of February 25, 2015. This time the initial sliding failures involved both the source area A and B (Figure 1) causing further retrogression of the headscarps, the complete mobilization of the earthflow, and the destruction of two earth berms. Further movements occurred in March 2015, then the landslide slowed down and almost stopped at the end of April 2015. The third and last reactivation was in May 25, 2015. Again, the landslide remobilized into a fluid, fast-moving earthflow that quickly reached the toe. Here local authorities removed the material 24 hours a day to save the houses. In June 2015, the earthflow almost stopped and significant consolidation works were carried out. Five earth berms were built across the landslide (Figure 1) and a trench drain system was realized to stabilize the middle-upper part of the slope. The landslide remained essentially stable in the following years with some localized slides in the source area and along the north flank.

Field observations provide qualitative but valuable information on the reactivation mechanism of the Montevecchio earthflow. In all the three cases, the mobilization starts with a relatively small translational slide in the source area (zones A-B-C; Figure 1) that occur during or shortly after rainstorms. In the source area the bedding planes dip with the same direction as the slope scarp at an angle of 40° with the horizontal, promoting slope instability by translational sliding and flexural buckling. The rock exposed on the scarp is an alternation of marly clay and fine sandstone, with estimated values of the uniaxial compressive strength in the range 1-5 MPa (measured in the field by simple index tests; *Hoek and Brown,* 1977). Although the rock is fresh or only slightly weathered, it completely disintegrates after rupture and turns into loose, fine-grained debris. The material detached from the scarp accumulates on the head of the gently inclined earthflow deposits causing ground bulging, cracks openings, and the formation of lateral shear surfaces. *Hutchinson and Bhandari* [1971] first introduced the term undrained loading to describe the failure of a saturated landslide deposit due to undrained compression and consequent rise of pore-water pressures.

After the initial slide, a surge of rapid movement can occur leading to the transformation of the earth slide into an earthflow. Evidence for this change in behavior includes: i) the landslide suddenly accelerates from millimeter-centimeters/day to meters/hour; ii) a variety of flow structures appear on the ground surface, such as arcuate pressure ridges parallel to the contour lines, hummocks, lateral levees, and tongue-shaped lobes; iii) the material softens by increasing the water content. This latter evidence is of particular interest. After each surge we surveyed the landslide and perform several simple tests to assess material softness by inserting a steel tube (5 cm diameter, 2 m long) into the ground. These qualitative data confirm that soon after a reactivation the earthflow is in a fluid state, at least within the upper 2 m. The material shows the consistency of a clay slurry, and we could easily insert the steel tube into the ground by hand throughout its length. Unfortunately, the depth of the fluidized layer remains unknown because the earthflow was not accessible to heavy machinery after a surge.

After the stage of rapid movement, the earthflow decelerates. The velocity at the toe and along the main track gradually decreases from m/day to cm/day, and the landslide continues to move within lateral shears zones with minor internal deformation. Interestingly, the material in the shear bands (20 to 40 cm thick) remain very soft for several weeks after the surge, while the landslide body becomes apparently stiffer and stronger.

4 Field data

4.1 In situ measurements of Rayleigh wave velocity

Methodology

We documented the reactivation of the Montevecchio earthflow by means of periodic and continuous measurements of Rayleigh wave velocities, carried out using two standard techniques: the active Multichannel Analysis of Surface Waves (MASW) [*Park et al.,* 1999] and the passive Refraction Microtremors (ReMi) techniques [*Louie,* 2001]. Both techniques exploit the properties of Rayleigh waves of different wavelengths to excite the material at different depths, thus travelling at different velocity: short wavelengths normally propagate slower (due to the lower velocity of shallow layers) while long wavelengths, which excite deeper layers, propagate faster [*Aki e Richards,* 1980*, Ben-Menahem and Singh,* 1981]. MASW focuses on the signal produced by artificial sources while ReMi exploits signals from natural sources.

The velocity of Rayleigh waves of different wavelengths into the ground is derived from the seismic signal recorded at different positions (a minimum of two) over time. Different mathematical algorithms can be used for this derivation. One of the simplest is to filter the signal at different frequencies and cross-correlate the filtered signal among all the geophone couples to find the time lag. Since the distance between each geophone couple is known, the propagation velocity can be obtained by dividing this distance by the time-lag. The result of the cross-correlation algorithm (normalized to the auto-correlation function) can be plotted in frequency-velocity plots as shown in the conceptual example of Figure 3.

Since the dispersion of surface waves is a multimodal phenomenon, different velocity values are possible at the same frequency, each one corresponding to a different propagation mode. In the case of an ideal source, ideal receiver geometry, and ideal material (homogeneous and isotropic half-space), the fundamental mode is dominant in terms of energy. However, in real cases this does not always happen. Selecting the dispersion curve of the fundamental mode or correctly sorting the higher modes implies a degree of subjectivity which represents one of the limits of the method as extensively discussed in the literature [*Gucunski and Woods,* 1992*; Tokimatsu et al.,* 1992*; Foti et al.,* 2014*; Castellaro,* 2016]. Here, we restrict the discussion to what can be inferred from Figure 3. The propagation velocity distribution of a surface wave at a specific frequency is given by the normalized cross-correlation function at that frequency. The graduated colour bar in Figure 3 represents the probability density distribution (in linear scale from 0 to 1) of the normalized cross-correlation function. The maxima of the distribution (blue dots in Figure 3) are the velocities associated with each frequency. The narrower the peaks (red shaded areas), the better the degree of accuracy of the velocity determination. The point A in Figure 3 indicates the Rayleigh velocity for a frequency of 30 Hz and the associated error bar, defined as the velocity range with a probability value higher than 0.8.

Rayleigh waves induce the maximum displacement in the subsoil at a depth which is approximately $z = \left| \frac{\lambda}{3}, \frac{\lambda}{2} \right|$, where λ is their wavelength and the range depends on the Poisson's ratio [*Jones*, 1962]. This approximate relation provides a way to determine both the velocity profile in the subsoil (remembering that $\lambda = V_R / f$, where the velocity V_R and the frequency f are those of Figure 3) and the maximum investigation depth. Refined inversion algorithms are available to evaluate the velocity profile with depth based on specific modeling of Rayleigh wave propagation in multilayered media exist, but are beyond the goal of this paper. Here we refer to the common approximation of converting wavelength to depth by using the relation $z = \lambda / 2.5$ [*Foti et al.*, 2014; *Castellaro*, 2016]. From this relation it also follows that the ideal aperture of the array is at least half the desired investigation depth $z_{max} / 2$ [*Rix and Leipski*, 1991; *Park et al.*, 2007], although arrays with $z_{max} / 4$ can still be effective under specific circumstances [*Castellaro*, 2016].

These standard techniques differ from the method used by *Mainsant et al.* [2012a] in a major aspect. *Mainsant et al.* [2012a] derived the velocity values in the subsoil from the cross-correlation of the signal between two geophones at known distance. The two geophones are planted in the stable ground on both sides of the landslide and provide the average Rayleigh velocity across the investigated section. Since the geophones are located outside the landslide, the system can operate even when the earthflow is rapidly moving. This is an important advantage compared to standard techniques that instead require access to the landslide area. However, the use of two geophones is appropriate only when the signal propagation is aligned with the geophone line. If this is not the case, the method provides apparent velocity values, larger than the real values by a factor $1/\cos\alpha$ where α is the angle between the signal propagation direction and the geophone alignment. The method can still provide correct results (that is an apparent velocity distribution centred on the real velocity value) provided that the noise distribution around the geophone line is homogeneous [*Mulargia and Castellaro*, 2013].
To overcome this limitation we decided to use standard methods by employing: a) active sources in line with the array, thus ensuring observation of real velocity values, b) a larger number of geophones, which allows one to compute more precise (statistically redundant) velocity values with depth, and c) in the case of purely passive surveys, where the source position with respect to the array is unknown, we examined several dispersion curves and retained in the analysis only those showing the lowest velocity values, which are by definition those closer to the real velocity values (given that $V_{apparent} = V_{real} / \cos\alpha$). Moreover, standard techniques provide measurements of Rayleigh velocity that allow comparing the state of the material in different locations along the landslide.

Periodic surveys

At Montevecchio, periodic measurements were done every 1-2 months (Tab. 1) along seven seismic lines. Four lines were located within the landslide area and three just outside the landslide as shown in Figure 4.

Table 1: Periodic seismic surveys carried out at Montevecchio (location of the measurement sections in Figure 4).

Date	**Measurement section**						
	A	B	C	D	E	F	G
2014/05/07	X	X	X	X	X	X	X
2014/06/06	X	X	X	X	X	X	X
2014/06/06	X	X	X	X	X	X	X
2014/07/27	X	X	X	X	X	X	X
2014/08/28		X	X	X			
2015/01/23		X	X	X			
2015/02/18			X				
2015/03/11		X	X	X			
2015/03/24		X	X	X			
2015/04/17		X	X	X			

2015/04/24	X	X	X	X			
2015/04/30			X		X	X	X
2015/05/07	X	X	X	X			
2015/05/19	X	X	X	X	X	X	X
2015/06/08	X	X	X	X			
2015/06/19		X	X	X			
2015/07/09	X	X	X	X			
2015/07/16		X	X				
2015/08/05	X	X	X	X			
2015/08/27			X				
2015/09/04	X	X	X	X			

We used six vertically polarized 4.5 Hz geophones, pressed firmly into the ground and set at intervals of 2 m each (total length of the seismic lines 10 m). A 10 m aperture antenna can detect waves as long as 40 m, which corresponds to maximum investigation depth of ~12. The first 5 minutes of each acquisition were done in the passive mode (ReMi), just acquiring the ambient seismic noise, while the last minute was in the active mode (MASW) by putting a seismic source (a jump of the operator) about 5 m apart from the first geophone, in order to ensure as planar as possible wavefronts at the geophones. All the geophones were connected to a Soilspy Rosina acquisition system and data were processed using the software Grilla (http://MoHo.world).

The data were analyzed to obtain the fundamental dispersion curves. Besides the problems generally related to the interpretation of dispersion curves (see above) the difficult field conditions provided further sources of uncertainty. During the dry season, the surface of the landslide was pervaded by desiccation cracks and open fractures (Figure 5a-b) and a firm coupling of the geophones with the ground was difficult. Conversely, during the rainy season or after the major reactivation events (Figure 5c) the material was fluid and most measuring points were not accessible. Both the variable ground conditions and the different location of the measuring points affected the accuracy of the results.

Figure 6 shows a typical Rayleigh-wave phase-velocity vs. frequency plot (spectrum) obtained at Montevecchio using active (Figure 6a) and passive (Figure 6b) methods. The dispersion curve can be traced by following the red-shaded areas of the frequency-velocity plots. In the active mode (Figure 6a) the dispersion curve is generally well defined over a wide range of frequencies and fundamental mode can easily be identified. In the passive mode (Figure 6b) the curve is discontinuous and the fundamental mode can be recognized only in some frequency intervals. For example, the dispersion curve shown in Figure 6b is not well defined around 10 Hz, from 13 to 17 Hz and above 25 Hz. In fact, active source methods are generally capable of resolving higher frequencies than passive methods because the source and receiver array can be tailored to the desired frequency range. On the contrary, the source for the ReMi survey was ambient seismic noise that typically contains significant low frequency energy and lacks high frequency signal, which can lead to poor resolution of shallow soil layers [*Louie*, 2001; *Cox and Wood*, 2010; *Strobbia and Cassiani*, 2011].

Continuous measurements

Periodic surveys were integrated by continuous measurements of surface wave velocity. To this aim, a cost-effective self-produced monitoring system was designed to include these features: 1) easy to install in the field and quick to remove; 2) low maintenance; 3) light enough to be carried by hand; 4) resistant to harsh field conditions (intense rainfall events, large ground displacements); 5) minimal energy consumption; 6) compatibility with other geotechnical sensors. A number of preliminary tests were conducted to find the optimal configuration. Different combinations of sampling rate (50 to 300 Hz), number of geophones (2 to 4) and duration of the acquisition session (from 30 s to 5 min) were tested in order to balance the desired signal accuracy with the capabilities of the datalogger and the power requirement. This appeared to be a suitable configuration for our needs: i) Campbell CR1000 data logger with CFM100 Compact Flash Module (2GB); ii) 4 vertical geophones at 4.5Hz with 4 signal amplifiers (gain=500); iii) power supplied by a 12 V 7 Ah battery recharged by a 20 W solar panel. Good results were obtained by reading the four geophones at 300 Hz for 2 minutes every 1 hour, thus simulating the execution of 24 ReMi surveys every day.

The monitoring system was installed at Montevecchio in May 16, 2014. The geophones were placed on the main track of the earthflow channel with a spacing of 2 m (Figure 4, blue line) and buried at a depth of 20 cm (Figure 7a-b) to avoid the atmospheric thermal effect and to ensure an adequate coupling with the ground [*Beekman,* 2008]. In the periodic surveys burial was not required because we hand-tamped around the geophones to ensure good coupling. The signals acquired with this type of approach require to be stable in time, implying a relatively constant background noise over the period of interest [*Hadziioannou et al.,* 2009]. Based on direct observation during the first field tests, the main source of ambient seismic noise vibration was the national road located at the toe of the landslide (about 400 m away from the monitoring system) which constitutes a spatially stable background noise. The data collected from the

datalogger were periodically downloaded and analyzed using the same software adopted for periodic surveys (Grilla).
Also in this case, dispersion curves were sometimes difficult to interpret, thus we decided to classify each curve as “good”, “fair”, or “bad” according to quality of the phase velocity spectrum (Figure 8). Figure 8a shows a dispersion curve classified as “good”: here the fundamental as well as a number of higher modes can clearly be distinguished in a wide frequency interval (5-50 Hz). The case (b) shows a “fair” dispersion curve in which the fundamental mode can be recognized only at low frequencies (5-10 Hz). Case c) shows a dispersion curve classified as “bad” because the fundamental mode cannot be detected. Bad curves are generally due to electrical problems with the signal amplifiers, cable ruptures, or bad ground coupling. For the purpose of the analysis, we only considered the “good” (a) or “fair” (b) dispersion curves. As representative velocity values, we picked the central points of the red range (which represents the highest probability range of velocity), while we used the red range boundaries (probability value higher than 0.8) to define the error bars (Figure 3).

Field monitoring was difficult and sometimes risky due to the strong landslide activity. Figure 7c-d shows the monitoring system just after the reactivation of February 25, 2015: all the equipment was moved downslope for about 100 m, the rain gage was destroyed and both the geophones and the amplifiers were lost. The landslide was not accessible for almost two months, not even to retrieve the equipment. The system was rebuilt and reinstalled on May 7, 2015. Less than one month later, the earthflow reactivated again and the monitoring system was again destroyed. During the monitoring period, we reinstalled the system six times because of the continuous landslide movements.

4.2 Landslide displacement

Landslide movement was measured using continuous GPS monitoring and a time-lapse camera. The GPS system consists of one reference station located in a stable area outside the landslide and three rover stations installed along the earthflow (Figure 4). Rover GPS devices were LEICA-GMX901 antenna (single frequency; 10 Hz update; horizontal accuracy: 3 mm + 0.5 ppm; vertical accuracy: 5 mm + 0.5 ppm) powered by two batteries (12 V 14 Ah in parallel) and recharged by a 60 W solar panel. Rover stations were equipped with Wi-Fi direction antennas (model Ubiquiti Nanostation M5) for transmitting data to the reference station. Both the GPS receiver, the control unit, and the WiFi antenna were installed on a 2 m long pole equipped with a helicoid tip that was screwed into the ground. The reference station was a dual-frequency LEICA GMX902 antenna connected to an industrial PC. The PC run the software Leica GNSS Spider used to process the data in real time. Power to the reference station was provided via a connection to the grid at 220 V. Raw data are processed in real time to determine the GPS coordinates of rovers in differential mode with respect to the reference station, i.e by calculating the baseline, which is the distance between rover and reference GPS antennas. Since the baseline of rover 1 (the one closest to the monitoring station) is nearly coincident with the direction of movement of the landslide, the measured displacements were not projected.

The time-lapse camera is a Brinno TLC200 that was placed outside the right flank of the earthflow (Figure 4) shooting the monitoring system. The camera has a focal length of 36 mm and it was set to take one picture every 30 minutes with a resolution of 640x480 pixels. An AVI video is created in the camera during recording, which results in a file of about 0.2 MB/frame stored on a 8 GB SD card. The analysis of these videos was carried out with the free software Tracker. The displacement was calculated knowing the dimension of an object in the camera view (a wood pole with red/white markings) and its distance from the camera. The pole was placed in the midline of the channel in order to measure the maximum velocity of the earthflow.

5 Results

5.1 Periodic acquisitions

Periodic seismic surveys were performed at Montevecchio from May 2014 to September 2015. For sake of clarity, we divide the dataset into the three periods that followed the three main reactivations.

Figure 9 illustrates the data collected after the first reactivation (May 2014-January 2015). The charts show the profiles of Rayleigh wave velocity (V_r) measured inside (section A, B, C, D) and outside (section E, F) the landslide area in the different campaigns (location in Figure 3). The dates of the seismic surveys are reported as days elapsed since the last mobilization (in this case the partial reactivation of April 27, 2014) in order to highlight the variation of V_r with time. As it can be seen, the Rayleigh wave velocity increased over time inside the landslide, while it remained constant outside. In particular, soon after the reactivation (10 days later) the landslide material was characterized by very low values of $V_r \approx 50$ m/s with no significant differences between the four sections. Then V_r increased. The rate of recovery along the earthflow was however different: in the source area (section A) it was faster than in the lower part (section D), whereas sections B and C showed intermediate values. For instance, in 271 days, the Rayleigh wave velocity at a depth of 5 m increased by 100, 45, 30, and 15 m/s moving from section A to D.

The data collected after the second reactivation (March to May 2015) provided similar results (Figure 10). The first survey was done only 14 days after the reactivation of February 25, when the landslide material was still partially fluid. The data show very low velocity profiles throughout the earthflow (see sections B, C, D; section A is missing because it was not accessible) revealing a sharp drop in V_r compared to initial conditions (end of the period in Figure 9). V_r remained low in the next two weeks due to the continuous movements of the earthflow, then gradually increased to the values shown before the mobilization. In this case, the recovery rate was similar in the three sections. The Rayleigh wave velocity outside the landslide remained constant and equal to that measured in the first period ($V_r \approx$200-250 m/s).

The data of the third period (June to September 2015) show a similar trend (Figure 11). Again, the lowest values of V_r occurred soon after the reactivation of May 25, 2015, then the wave velocity increased to the initial value. During this third period the variation of V_r with time was quite complex (especially in sections B and C) because of the extensive consolidation works carried out from July to September 2015, that triggered partial reactivations of the earthflow around the construction area of the earth berms. The last survey was on September 4, 2015. After that, local authorities installed a dense network of trench drains and drainage channels to stabilize the landslide and most of the material was reworked up to a depth of 2-4 m.

The chart in Figure 12 summarizes the data collected inside and outside the landslide area over the whole period. For this comparison, we used the Rayleigh wave velocity measured at a depth of 2 m, where the dispersion curves are well defined. Despite the difficulties posed by the harsh field conditions and the uncertainties in these geophysical measurements, a clear trend emerges from the data: the Rayleigh wave velocity dropped to very low values as the earthflow reactivated, then it increased to the initial values following a non-linear trend.

5.2 Continuous monitoring

Continuous monitoring was designed to capture the change in material properties during the mobilization of the earthflow. The Montevecchio monitoring system was installed in May 2014 (after the first reactivation of February 12014) and recorded the second and third reactivation. The third reactivation of May 25, 2015 is the best documented being both the GPS and the time-lapse camera active. Figure 13 shows the data collected three weeks before and after this event. The red and blue dots indicate the Rayleigh wave velocity at a frequency of 11 and 15 Hz, which correspond to an approximate depth of 1 and 2 m respectively. The gray dots are the velocities at 8 Hz (approx. 3 m). The investigation depth is restricted to the first meters because the dispersion curves obtained by the monitoring system are poorly represented for low frequencies (section 4.1). However, since the velocity profiles obtained by the periodic surveys are almost linear with depth and vary evenly over time (Figure 11), we believe that these data are representative of the general behavior of the landslide.

In the first three weeks of May 2015, the landslide was slowly moving at a rate of less than 1 cm/day. Rayleigh velocities were fluctuating around 50-55 m/s, as typically observed during the suspended state of activity of the landslide. On May 22, it started to rain at 01:10 AM and continued until May 24 08:40 AM with 47 mm in 56 hours. About 11 hours after the beginning of the rain (small inset in Figure 13a) the landslide started to accelerate and the displacement rate increased by five times (from 0.8 cm/day to 4 cm/day, Figure 13b). The Rayleigh velocity dropped to 30-35 m/s (30% drop) and remained low for the next two days May 23 and 24, until the first surge of rapid movement (Figure 13c). The first surge started around midnight on May 24, 16 hours after the end of the rain: the landslide quickly accelerated to 5.8 m/day and reached the peak velocity of 10 m/day (200 times higher than the day before) in the morning of the 25. In a few hours the earthflow moved downslope of 5-7 m disrupting the geophones array. The landslide then slowed down and the velocity decreased to 1.2 m/day in the following 10 hours. A second rainfall event of 24 mm in 3 hours occurred on May 26 05:30 PM, leading to the complete reactivation of the earthflow. This second surge lasted three days with a peak velocity of 22 m/day and a total displacement of about 35 m. The geophones were buried by the landslide and most of the equipment was destroyed.

The monitoring system was reinstalled on June 3, 2015. The data collected after the surges confirm the results of periodic surveys, showing an increase of Rayleigh velocities as the landslide decelerates. Three weeks after the reactivation, V_r almost returned to the initial values of 50-60 m/s. Rayleigh velocities remained essentially constant until the end of July 2015 (Figure 14). On July 26, the local authorities started to build an earth dam in the source area A (location in Figure 1) causing a partial reactivation of the landslide. The monitoring system recorded an increase of the displacement rate (from about 5 cm/day to 40 cm/day) accompanied by a decrease in V_r of about 20% (Figure 14c). Again, V_r increased to 50-60 m/s as the earthflows decelerates.

Figure 15 shows the data collected during the second reactivation of February 25, 2015. The general trend depicts a progressive increase of the displacement rate (Figure 15a-b) accompanied by a decrease of the Rayleigh velocity (Figure 15c). However, a closer look shows some complexity. Rayleigh velocity started to decrease below its normal range on January 31, while the landslide was slowly moving at a constant speed of about 5 cm/day. Time lapse videos revealed that in those days the ground started to bulge due to the rapid loading of an upload slide. In the next days the Rayleigh velocity remained low (around 45 m/s) and essentially constant, although the displacement rate increased in response to the rainfall event of February 3-6 (160 mm in 4 days). The lowest values of Rayleigh velocity (less than 40 m/s) were recorded anyway just before the complete reactivation of February 25.

Figure 16 shows the data recorded five months after the first surge, during a long stage of suspended activity (July to November 2014). In that period, the landslide was moving very slowly (Figure 16a) with a trend of slightly decreasing velocity(few mm/day, Figure 16b). As expected, the Rayleigh velocities remained essentially constant with small fluctuations around 50 m/s (Figure 16c). The temporary accelerations exhibited by the landslide in response to the rainfall events did not cause any detectable decrease of Rayleigh velocity.

6 Discussion

The data collected at Montevecchio indicate that the mechanical properties of the earthflow material change during surges. The periodic measurements of Rayleigh wave velocity (Figure 9-11) provide the clearest evidence of this variation. Soon after a surge, the values of V_r are very low within the entire thickness of the flowing mass, then they gradually increase through time as the landslide decelerates. The general trend is similar for the three reactivations and across the landslide (Figure 12), although the absolute values of V_r and the rate of recovery are quite different. Possible reasons for these differences are the variable thickness of the landslide, the influence of partial reactivations, the different rate of residual movement, and the effect of consolidation works. For instance, the construction of an earth berm close to section A (Figure 1) is the reason for the rapid increase of V_r observed in that area after the first reactivation (Figure 9A), while the continuous excavations carried out at the toe of the landslide explain the low rate of recovery in section D (Figure 9D).

Figure 17a provides an overall view of the data collected by periodic surveys. Each point shows the mean Rayleigh velocity measured at a depth of 2 m inside (sections A to D) and outside (sections E and F) the landslide area. Time is reported as number of days elapsed since the last surge. The chart shows that inside the earthflow the Rayleigh velocity increases with time of 30-40% following a power function. A strong increase of V_r occurs in the first 50-70 days after a reactivation, then the velocity seems to attain a constant value (though the curve is not well constrained in the long term). Outside the landslide area, V_r is constant and remarkably higher. These data can be interpreted according to the general theory of surface wave propagation. Rayleigh waves travel with a horizontal wave speed V_r slightly lower than the shear wave speed V_s. The ratio V_r/V_s is a function of the material's Poisson ratio ν [*Achenbach*, 2012]:

$$\frac{V_r}{V_s}=\frac{0.862+1.14\nu}{1+\nu} \tag{1}$$

varying from 0.90 for $\nu=0.5$ (soft soils in undrained conditions) to 0.95 for $\nu=0.2$ (stiff soils in drained conditions). In an elastic solid, the velocity of a shear wave is controlled by the solid's density (ρ) and shear modulus (G_0):

$$V_s=\sqrt{\frac{G_0}{\rho}} \tag{2}$$

where the notation G_0 indicates the initial shear modulus at very small strains (0.001% or less). Since the density ρ has a negligible effect on V_s compared to G_0, the observed variation of Rayleigh velocity at Montevecchio can be interpreted as a change in the shear stiffness of the earthflow material. Figure 17b shows the values of G_0 computed from the shear velocity assuming $\nu = 0.5$ and constant soil density $\rho = 1600$ kg/m^3 (taken as the average between the density at the liquid limit $\rho \approx 1400$ kg/m^3 and the average density measured in the field $\rho \approx$ 1800 kg/m^3). As can be seen, the shear modulus of the earthflow material is very low soon after mobilization ($G_0 \approx 5$ MPa) then increases up to 15-20 MPa in a few months. This change in shear stiffness suggests a transition from a very soft to a stiff clay [*Ortiz et al.*, 1986].

Similar results are obtained using undrained shear strength (s_u). A number of V_s-based correlations have been proposed in the literature to estimate s_u. *Mayne* [2007] derived a generalized relation between shear wave velocity and cone tip resistance (q_t in kPa) suitable for clay materials from soft to firm:

$$V_s = 1.75 q_t^{0.627} \tag{3}$$

Nguyen et al. [2014] found a correlation between G_0 and net cone tip resistance ($q_t - \sigma_{v0}$, where σ_{v0} is the total vertical stress) better constrained for soft clays:

$$G_0 = 89.1(q_t - \sigma_{v0})^{1.50} \tag{4}$$

These relationships can be inverted to obtain q_t and combined with the classical formula $s_u = (q_t - \sigma_{v0}) / N_{kt}$ (where $N_{kt} \approx 14$ is a bearing factor; *Robertson*, 2009) to get an estimate of undrained strength. The results obtained with the two formulas (using V_s from 64 to 109 m/s in equation (3), and G_0 from 7 to 19 MPa in equation (4)) are similar: the undrained strength is as low as 10-20 kPa soon after reactivation and increases up to 30-50 kPa in a few months. Two cone penetration tests carried out at the toe of the earthflow three weeks after the first reactivation confirm these estimates: in the first 8 m, the tests show a uniform profile of s_u with depth with average values in the range 15-20 kPa. According to the British Standard 5930 [*BSI*, 2015], this change in strength indicates the transition from a very soft to a firm clay.

The data collected by the monitoring system provide evidence of changes in the material properties before a surge. Rayleigh velocity decreases about 20-30 m/s (about 30% of the initial value) just before the rapid movements of February and May 2015 (Figure 13-15), indicating that the material softened as the earthflow approached a new reactivation. The observed drop is about 10 times larger than the standard deviation of measurements computed when the landslide is not moving (2.2 m/s obtained as the average of the standard deviations calculated for the three frequencies in Figure 16). However, the relationship between displacement rate and Rayleigh velocity is not simple. In particular, there is no correlation between landslide speed and V_r drop (apparently, V_r decreases a similar amount regardless of the velocity attained by the landslide) and also the timing of the drop may differ (section 5.2). Unfortunately, available data do not allow one to establish why there are these differences, mostly because of the limited accuracy of the measurements. A series of tests conducted in the field showed that the dispersion curve obtained without an active seismic source, and using only 4 geophones instead of the 6 used in periodic surveys, is often discontinuous or poorly defined. This makes it difficult to detect the Rayleigh velocity of the fundamental mode and introduces significant uncertainties in the data.

Despite these uncertainties, the data seem to provide a consistent picture: the earthflow material softens during a surge, and then recovers to the initial state when the velocity decreases and the landslide comes to rest. The observed behavior cannot be explained by a simple sliding mechanism in which the landslide moves as a plastic solid. The drop in shear stiffness clearly plays an important role in the rapid movement of the Montevecchio earthflow.

What is now more difficult to establish is whether the measured variation of V_r may indicate a solid-to-fluid transition of the earthflow. In principle, we could infer the void ratio e of the material from the shear stiffness G_0, and compute the gravimetric water content at saturation w ($w = e/G_s$, where $G_s \approx 2.7$ is the specific gravity of solids) in order to evaluate the state of the earthflow. However, going from Rayleigh velocities to void ratio is fraught with uncertainties, mostly because the various forms of the $G_0 - e$ functions published in the literature might not apply to our field conditions. In particular, the measured change of Rayleigh velocity at Montevecchio could be due to the opening (or closing) of fissures and cracks within the earthflow rather than dilation (or contraction) of the soil skeleton. The following analysis therefore provides only a rough estimate of e and should be taken with care.

Santos and Correia [2000] compared a number of empirical $e - G_0$ relationships and proposed the following function for soils with high percentages of fines:

$$G_0 = 4000 e^{-1.3} p^{0.5} \tag{5}$$

where p is the mean effective stress. Inverting the equation and assuming $p \approx \sigma'_{v0} = 12$ kPa (effective vertical stress at a depth of 2 m considering $\rho = 1600$ kg/m^3 and water table at the ground surface) we can estimate e from G_0. According to equation (5) the observed increase of shear stiffness after a surge (G_0 from 5 to 20 MPa) corresponds to a decrease of void ratio from $e \approx 2$ to $e \approx 0.7$. The equivalent change in terms of gravimetric water content is from w≈80% to w≈30%. By comparing these values with the Atterberg limits (plastic limit PL=26%; liquid limit LL=50%) it turns out that the water content of the earthflow material is well above the liquid limit soon after a surge and close to the plastic limit a few months later. These results are consistent with the field evidence of a fluidized surface of the earthflow that becomes stiffer with time (section 3).

The change of void ratio with time is of particular interest because it allows a quantitative analysis of observed behavior. Figure 18 shows this trend using a normalized void ratio index ($\hat{e}$) that depicts the relative variation of e with respect to the minimum and maximum values estimated above ($e_{\min}$=0.7 and $e_{\max}$=2):

$$\hat{e} = \frac{e_{\max} - e}{e_{\max} - e_{\min}} \tag{6}$$

The trend of the experimental points is consistent with the exponential decrease of pore volume (and increase of material stiffness) that occurs with time during the consolidation of a porous material. In fact, it agrees well with the theoretical trend (red curves in Figure 18) predicted by the one-dimensional consolidation theory [*Terzaghi,* 1943]. Terzaghi's consolidation theory allows one to compute the change in void ratio of the soil skeleton to the change in effective stress by means of a coefficient of consolidation (c_v) determined in the oedometer test. The theoretical curves in Figure 18 are computed using typical values of c_v for fine-grained material [*Holtz and Kovacs*, 1981]. These simple calculations suggest that the Montevecchio earthflow is in a fluid state soon after a rapid stage of movement and returns to a plastic state as the material consolidates.

A further point of discussion is the possible use of this technique for early- warning of earthflow movement. *Mainsant et al.* [2012a] detected a decrease of the relative Rayleigh wave velocity well before the reactivation of their monitored landslide (a first 2% drop about one month before the movement, and a second 7% drop four days before). *Mainsant et al.* [2015] carried out some laboratory experiments on artificial clay slopes having different water content and confirmed a drop in V_r values before the failure. Based on these the authors suggested that field monitoring of surface wave velocity could be potentially used to predict landslides [*Mainsant et al.,* 2012a].

These results are more uncertain. Also in our case the Rayleigh velocities start to drop a few days before a surge (Figure 13 and 15) but the relationship between V_r and landslide speed is not straightforward. Besides the uncertainty in the data (as discussed above), a possible explanation is that we started to monitor the landslide after a major reactivation (February 2014) that completely remobilized the existing deposits, generating a dense network of pervasive cracks and fissures within the landslide mass. The two surges of February and May 2015 were subsequent reactivations of a completely remolded material. In these conditions, the effect of pre-failure cracking and deformations is probably negligible, and we could only detect the main changes in shear stiffness associated with the very rapid movements. Therefore our data cannot prove (or disprove) the use of Rayleigh wave monitoring for early landslide detection.

Finally, we comment on the technique adopted at Montevecchio for the continuous monitoring of Rayleigh wave velocity. The system configuration (4 vertical geophones at 4.5 Hz; 2 min sessions at 300 Hz every 1 hour; passive mode) proved its effectiveness, but with a low accuracy compared to periodic surveys. Several modifications can be done to improve results: 1) combine active and passive mode acquisition in order to improve the dispersion curve at high frequency ranges (for example, using an automatic hammer controlled by the datalogger that hits the ground during the measurement session); 2) use more geophones to ensure an adequate data redundancy [*Tokimatsu,* 1997]. As an alternative to surface wave monitoring, one could use a down-hole probe specifically designed for long-term monitoring in order to get direct measurements of shear wave velocity inside an active landslide. A further improvement is to combine geophysical data with geotechnical sensors to monitor the water content of the material. Conventional dieletric sensors have an accuracy of 2-3% [*Starr and Paltineanu,* 2002] and should easily detect the dramatic change of water content required for the earthflow to transition to a liquid state.

7 Conclusions

Rayleigh wave monitoring proved to be an effective method to investigate changes in material properties that occur in active earthflows. In this study, we monitored rainfall, ground displacement, and Rayleigh wave velocity of an earthflow located in the Northern Apennines of Italy during a two-year period of intense activity. Based on these data, several conclusions can be drawn:

1. As the earthflow accelerates approaching a stage of rapid movement, the material exhibits a significant drop of Rayleigh wave velocity (V_r); V_r then gradually increases through time as the landslide decelerates, returning to the initial values in a few months.

2. The observed variation of Rayleigh velocity indicates that the earthflow material undergoes a significant change in shear stiffness and undrained strength during each reactivation.

4. A simple mechanism of rigid-block sliding cannot account for the observed changes of material properties; therefore, internal disturbance and remolding play an important role in the dynamics of the Montevecchio earthflow.

5. Tentative estimates of the gravimetric water content suggest that the earthflow material is well above the liquid limit soon after a surge and decreases with time to the plastic limit following a non-linear trend typical of a consolidation process; these estimates are consistent with the field evidence of a fluidized surface of the earthflow that becomes stiffer with time.

6. At Montevecchio, there is no clear evidence that Rayleigh velocity starts to decrease well before the landslide starts to move, as found by *Mainsant et al.* [2015]. However, in our case the material was completely remolded by previous movements, thus we probably missed the initial cracking that occurs when the landslide reactivates after a long period of dormancy.

7. Because of the difficult field conditions and limited accuracy of the data, available measurements do not allow the precise identification of the relationship between rainfall, displacement rate, and Rayleigh velocity. In order to get better results from field monitoring we suggest the use of 6-8 geophones (instead of 4), the use of an active seismic source controlled by the data logger, and installation of soil moisture sensors at different depths for direct measurement of water content inside the landslide.

Acknowledgments

This work was supported by the Civil Protection Agency of the Emilia-Romagna Region under the framework agreement “Special activities on support to the forecast and emergency planning of Civil Protection with respect to hydrogeological risk” (ASPER-RER, 2011–2015 and 2016-2021). The authors would also like to acknowledge the Editor, the Associate Editor, and the anonymous reviewers of JGR, who provided constructive comments and suggestions which improved the quality of the paper. All the data used in this paper are listed in the references or are included in the figures and tables.

References

Achenbach, J.D. (2012). *Wave propagation in elastic solids*. Amsterdam, The Netherlands: Elsevier.

Aki, K., & Richards, P. G. (1980). *Quantitative seismology, Theory and Methods*. San Francisco: W. H. Freeman & Co. DOI10.1017/S0016756800034439

Ancey, C. (2007). Plasticity and geophysical flows: A review. *Journal of Non-Newtonian Fluid Mechanics, 142*(3), 4-35.

Baum, R.L., Savage, W.Z., & Wasowski, J. (2003). *Mechanics of Earth Flows*. Paper presented at International Workshop on Occurrence and Mechanisms of Flows in Natural Slopes and Earthfills, Sorrento, Italy.

Beekman, A.N. (2008). *A comparison of experimental ReMi measuraments with various source, array, and site condition*, (master's thesis). University of Arkansas.

Ben-Menahem, A., & Singh, S.J. (1981). *Seismic waves and sources*. New York: Springer-Verlag.

Berti, M., Martina, M.L.V., Franceschini, S., Pignone, S., Simoni, A., & Pizziolo, M., (2012). Probabilistic rainfall thresholds for landslide occurence using a Bayesian approach. *Journal of Geophysical Research*, *117*, 1-20.

Bovis, M.J., & Jones, P. (1992). Holocene history of earth flow mass movement in South central British Columbia: the influence of hydroclimatic changes. *Can. Journal Earth Sci., 29*, 1746-1755.

BSI (2015). *BS 5930: 2015—The Code of Practice for Site Investigations*. British Standards Institute, Milton Keynes.

Casagrande, A. (1932). Research on the Atterberg Limits of Soils. *Public Roads*, *13*(8), 121–136.

Castellaro S. (2016). Soil and structure damping from single station measurements. *Soil Dynamics and Earthquake Engineering*, *90*, 480-493.

Coe, J.A., McKenna, J.P., Godt, J.W., & Baum, R.L (2009). Basal-topographic control of stationary ponds on a continuously moving landslide. *Earth Surf. Process. Landf., 34*, 264-279.

Coussot, P., Laigle, D., Arattano, M., Deganutti, A., & Marchi, L. (1998). Direct Determination of Rheological Characteristics of Debris Flow, *Journal of Hydraulic Engineering*, *124*(8), 865-868.

Cox, B.R., & Wood, C.M. (2010). *A comparison of linear array surface wave methods at soft soil site in the Mississippi Embayment*. Paper presented at GeoFlorida 2010, Orlando, Florida.

Craig, D. (1979). *Some apsects of mudslide stability in East County Antrim, Northern Ireland*, (Doctoral thesis). Queen's University of Belfast, Ireland.

Cruden, D.M., & Varnes, D.J. (1996). Landslide types and processes. In: Turner, A.K. and Shuster, R.L. (Eds.), *Landslides: Investigation and Mitigation*, (Special Report No. 247, 36-75), Washington: National Academy Press.

D'Elia, B., Picarelli, L., & Leroueil, S. (1998). Geotechnical characterization of slope movements in structurally complex clay soils and stiff jointed clays. *Rivista Italiana di Geotecnica*, *33*, 5-32.

Foti, S., Lai G. C., Rix G. J., & Strobbia C. (2014). *Surface wave methods for near-surface site characterization*. London: CRC Press.

Giordan, D., Allasia, P., Manconi, A., Baldo, M., Santangelo, M., Cardinali, M., Corazza, A., Albanese, V., Lollino, G., & Guzzetti, F. (2013). Morphological and kinematic evolution of a large earthflow: The Montaguto landslide, Southern Italy. *Geomorphology*, *187*, 61-79.

Gucunski, N, & Woods, R.D. (1992). Numerical simulation of the SASW test. *Soil Dyn. Earthq. Eng.*, *11*, 213–27.

Hadziioannou, C., Larose, E., Coutant, O., Roux, P., & Campillo, M. (2009). Stability of monitoring weak changes in multiply scattering media with ambient noise correlation: Laboratory experiments, *J. Acoust. Soc. Am*., *125*(6), 3688–3695.

Handwerger, A. L., Roering, J.J., & Schmidt, D.A. (2013). Controls on the seasonal deformation of slow-moving landslides. *Earth and Planetary Sciences Letters*, 377-378.

Hang, P. T., & Brindley G.W. (1970). Methylene blue absorption by clays minerals. Determination of surface areas and cation exchange capacities (clay organic studies XVIII). *Clays and clay minerals*, *18*(4), 203-212.

Hoek, E., & Brown, E.T. (1977). Practical estimates of rock mass strength. *International Journal of Rock Mechanics and Mining Sciences*, *34*(8), 1165-1186.

Holtz, R.D. & Kovacs, W.D. (1981). *An Introduction to Geotechnical Engineering*. Civil Engineering and Engineering Mechanics Series, New Jersey: Prentice-Hall.

Hungr, O., Evans, S.G., Bovis, M.J., & Hutchinson, J.N. (2001). A review of the classification of landslides the flow type. *Environ. Eng. Geosci., 7*, 221–238.

Hutchinson, J.N. (1970). A coastal mudflow on the London clay cliffs at Beltinge, North Kent. *Geotechnique*, *20*(4), 412-438.

Hutchinson, J.N. & Bhandari, R.K. (1971). Undrained loading, a fundamental mechanism of mudflows and other mass movements. *Geotechnique*, *21*(4), 353-383.

Hutchinson, J. N., Prior, D. B., & Stephens, N. (1974). Potentially dangerous surges in an Antrim [Ireland] mudslide: *Quarterly Journal of Engineering Geology*, *7*(4), 363-376.

Hutchinson, J.N. (1988). *General report: morphological and geotechnial parameters of landslides in relation to geology and hydrogeology*. Paper presented at Fifth International Symposium on Landslides, Rotterdam, Netherlands.

Iverson, R.M., & Major, J.J. (1987). Groundwater seepage vectors and potential for hillslope failure and debris flow mobilization. *Water Resources Research*, *22*(11), 1543-1548.

Jones, R. (1962). Surface wave technique for measuring the elastic properties and thickness of roads: Theoretical development. *British Journal of Applied Physics*, *13*(1), 21-29.

Jongmans, D., Baillet, L., Larose, E., Bottelin, P., Mainsant, G., Chambon, G., & Jaboyedoff M. (2015). *Application of ambient vibration techniques for monitoring the triggering of rapid landslides*. Paper presented at *Engineering Geology for Society and Territory*, Torino, Italy.

Keefer, D.K., & Johnson, A.M. (1983). *Earthflows: morphology, mobilization and movement*. U.S. Geological Survey Professional Paper (1264), U.S. Government Printing Office.

Lautrin, D. (1989). Utilisation pratique des parametres derives de l'essai au blue de methylene dans le les projets de genie civile. *Bulletin de Liaison des laboratories des ponts et Chaussees*, *160*, 29-41.

Louie, J.N. (2001). Faster, better: shear-wave velocity to 100 meters depth from refraction microtremor arrays. *Bulletin of Seismological Society of America*, *91*(2), 347-364.

Mainsant, G., Larose, E., Bronnima, C., Jongmans, D., Michoud, C., & Jaboyedoff, M. (2012a). Ambient seismic noise monitoring of a clay landslide: toward failure prediction. *Geophisical Research Letters*, *117*, 1-12. https://doi.org/10.1029/2011JF002159.

Mainsant, G., Jongmans, D., Chambon, G., Larose, E., & Baillet, L. (2012b). Shear-wave velocity as an indicator for rheological changes in clay materials: Lessons from laboratory experiments. *Geophysical Research Letters*, *39*(19), 1-5.

Mainsant, G., Chambon, G., Jongmans, D., Larose, E., & Baillet, L. (2015). Shear-wave-velocity drop prior to clayey mass movement in laboratory flume experiment. *Engineering Geology*, *192*, 26-32.

Mayne, P., (2007). *Cone Penetration Testing, a synthesis of highway practice*. Washington D.C.: Trasportation Research Board.

Moore, R. (1988). *The clay mineralogy, weathering and mudslide behaviour on coastal cliffs*, (Doctoral thesis). King's College, University of London.

Mulargia F., & Castellaro S. (2013). A seismic passive imaging step beyond SPAC and ReMiTM. *Geophysics*, *78*, 63-72.

Nguyen, H.Q., DeGroot D.J. & Lunne T. (2014). *Small strain shear modulus of marine clays from CPT*. Paper presented at 3rd International Symposium on Cone Penetration Testing, Las Vegas, Nevada, USA.

Ortiz,M., & Simo, J.S. (1986). An analysis of a newclass of integration algorithms for elastoplastic constitutive relation. *Int. Jou. Numerical Methods in Engineering*, *23*(3), 353-366.

Park, C., Miller, R., & Xia, J. (1999). Multi-channel analysis of surface waves. *Geophysics*, *64*(3), 800-808.

Park, C. B., Miller, R. D., Xia, J., & Ivanov, J. (2007). Multichannel analysis of surface waves (MASW) —Active and passive methods. *The Leading Edge*, *26*(1), 60–64.

Pastor, M., Blanc, T., & Pastor, M.J. (2009). A depth integrated viscoplastic model for dilatant saturated cohesive-frictional fluidized mixitures: Application to fast catastrophic landslides. *Journal of non-Newtonian fluid mechanics*, *158*(1-3), 142-153.

Pastor, M., Manzanal, D., Fernandez Merodo, J.A., Mira, P., Blanc, T., Drempetic, V., Pastor, M.J., Haddad, B., & Sanchez, M. (2010). From solids to fluidized soils: diffuse failure mechanisms in geostructureswith applications to fast catastrophic landslides. *Granular Matter*, *12*(3), 211-228.

Picarelli, L., Urcioli, L., Ramondini, G., & Comegna, L. (2005). Main features of mudslides in tectonised highly fissured clays shales. *Landslides*, *2*(1), 15-30.

Prior, D.B., Stephens, N., & Archer, D.R. (1968). Composite mudflows on the Antrim coast of north east Ireland. *Geografiska Annaler*, *50*(A), 65-78.

Reynolds, J.M. (1997). *An introduction to applied and environmental geophysics*. Chichester: John Wiley.

Ricci Lucchi, F., Bassetti, M.A., Manzi, V., & Roveri, M. (2002). Il Messiniano trent'anni dopo: eventi connessi alla crisi di salinità dell'avanfossa appenninica. *Studi Geol. Camerti*, *1*, 127-142.

Richart, F. E., Hall, J. R., & Woods, R. D. (1970). *Vibrations of soils and foundations.* Englewood Cliffs, NJ: Prentice-Hall, Inc.

Rix, G. J., & Leipski, E.A. (1991). Accuracy and resolution of surface wave inversion. In: Bhatia, S. K., and Blaney, G. W. (Eds.), *Recent advances in instrumentation, data acquisition and testing in soil dynamics,* Am. Soc. Civil Eng., San Diego, CA.

Robertson, P.K. (2009). Evaluation of flow liquefaction and liquefied strengh using the cone penetration test. *Journal of Geotechnical and Geoenvironmental Engineering*, *136*(6), 842-853.

Robertson, P.K. (2010). *Estimating in situ state parameter and friction angle in sandy soils from CPT*. Paper presented at 2nd Internation Symposium of Cone Penetration Test, Signal Hill, California, USA.

Santos, J.A, & Correia, G. (2000). *Shear modulus of soils under cyclic loading at small and medium strain level*. Paper presented at 12WCEE 2000, Auckland, New Zeland.

Schadler, W. (2010). *Slope movements of the earthflow type - engineering -geological investigation, geotechnical assessment, and modelling of the source areas on the basis of case studies from the Alps and Apennines*. Berlin: Logos verlag Berling GmbH.

Schulz, W. H., Mackenna, J. P., Kibler, J. D., & Biavati, G. (2009). Relations between hydrology and velocity of a continuously moving landslide – evidence of pore pressure feedback regulating landslide motion? *Landslides*, *6*, 181-190.

Seed R.B., Cetin K.O., Moss. R.E.S., Kammerer, A.M., Wu, J., Pestana, J.M., Riemer, M.F., Sancio R.B., Bray J.D., Kayen R.E., & Faris, A. (2003). *Recent advances in soil liquefaction engineering: a unified and consisted framework*. Eartquake Engineerig Research Center, Report No. EERC 2003-6, California, USA.

Simoni, A., Ponza, A., Picotti, V., Berti, M., & Dinelli, E. (2013). Earthflow sediment production and Holocene sediment record in a large apenninic catchment. *Geomorphology*, *188*, 42-53.

Starr, J.L. & Paltineanu, I.C. (2002). Methods for measurement of soil water content: Capacitance devices. In: Dane J.H., Topp G.C., (Eds), *Methods of Soil Analysis: Part 4 Physical Methods*. Madison, WI: Soil Science Society of America.

Strobbia, C., & Cassiani, G. (2011). Refraction microtremors: Data analysis and diagnostics of key hypotheses. *Geophysics*, *76*(3), MA11-MA20.

Telford M.W., Geldart, L. P., & Sheriff, E.R. (1990). *Applied geophysics*. Cambridge: Cambridge University Press.

Terzaghi, K. (1925). *Erdbaumechanik auf Bodenphysikalischer Grundlage*. Franz Deuticke, Liepzig-Vienna.

Terzaghi, K.,(1943). *Theoretical Soil Mechanic*. New York : John Wiley and Sons.

Tokimatsu, K., Tamura, S., Kojima, H. (1992). Effects of multiple modes on Rayleigh wave dispersion characteristics. *Journal Geotech. Eng*., *118*, 1529–43.

Tokimatsu, K. (1997). *Geotechnical site characterization using surface waves*. Paper presented at 1st Intl. Conf. Earthquake Geotechnical Engineering, Tokyo.

Van Asch, T. W. J., & Malet, J.P. (2009). Flow-type failures in fine-grained soils: an important aspect in landslide hazard analysis. *Nat. Hazards Earth Syst. Sci., 9*(5), 1703–1711.

Varnes, D.J. & Savage, W.Z. (1996). *The Slumgullion earth flow: a large scale natural laboratory*. U.S Geological survey bulletin (2130), U.S. Government Printing Office.

Figure Captions

Figure 1. Geological map of the study area. The capital letters (A, B and C) indicate the source areas of the Montevecchio earthflow. The red line shows the boundary of the landslide in July 2015. The colored dotted lines show the three reactivations and the evolution of the headwall scarp in source areas A and B.

Figure 2. Photographs of the Montevecchio earthflow in July 2015. a) panoramic view of the source area A with the upper part of the earthflow channel; b) main reach of the earthflow channel; c-d) deposition area after the second reactivation of February 2015.

Figure 3. Conceptual example of the MASW/ReMi analysis. Top left: schematic geophone array (G1-G6). Top right: flowchart of the solving algorithm. Bottom: frequency-velocity plot showing the experimental propagation velocity distribution of a surface wave at a specific frequency. The graduated colour bar shows the probability density distribution of the normalized cross-correlation function; the blue dots indicate the most probable velocity values for each frequency. The point A indicates the Rayleigh velocity for a frequency of 30 Hz and the associated error bar, defined as the velocity range with a probability value higher than 0.8.

Figure 4. Map showing the location of the monitoring system and periodic seismic surveys.

Figure 5. Photographs showing the difficult ground conditions encountered during periodic seismic surveys. a-b) cracks and open fractures characterize the landslide surface during the dry period; c) water ponds and soft soil reduce the accessibility soon after a reactivation or an intense rainfall.

Figure 6. Rayleigh-wave phase-velocity spectra acquired on January 23 2015 along section C (a=active survey; b=passive survey). Numbers 1 to 8 indicate the geophones.

Figure 7. Photographs of the Montevecchio monitoring system. a) geophone amplifiers inserted in a plastic box; b) continuous monitoring system installed in the main track of the earthflow channel. c-d) equipment damaged by a reactivation of the earthflow.

Figure 8. Example of three dispersion curves acquired by the monitoring system. These curves were classified as ‘good’ (a), ‘fair’ (b), and ‘bad’ (c) according to the quality of the phase velocity spectrum (see text). Numbers 1 to 8 indicate the geophones. The graduated colour bars show the probability density distribution of the normalized cross-correlation function.

Figure 9. Rayleigh wave velocity profiles measured after the reactivation of April 27, 2014 inside (A, B, C, D) and outside (E, F) the landslide. Note the change in scale between A-D and E-F. Locations of each site are shown in Figure 4.

Figure 10. Rayleigh wave velocity profiles measured after the reactivation of February 25, 2015 inside (B, C, D) and outside (E) the landslide. Note the change in scale for site E. Sites F and G (located outside the landslide) are not shown because the Rayleigh velocity profiles remained constant. Locations of each site are shown in Figure 4.

Figure 11. Rayleigh wave velocity profiles measured in the period June 2015-September 2015 inside the landslide. Sites F and G (located outside the landslide) are not shown because the Rayleigh velocity profiles remained constant. Locations of each site are shown in Figure 4.

Figure 12. Variation of Rayleigh wave velocity with time during the whole period of measurement. Each point indicates the value measured at a depth of 2 m. Arrows show the start of the main reactivation events of the earthflow.

Figure 13. Comparison between (a) rainfall and cumulative displacement, (b) displacement rate and (c) Rayleigh velocity measured by the monitoring system before and after the reactivation of May 25, 2015.

Figure 14. Comparison between (a) rainfall and cumulative displacement, (b) displacement rate and (c) Rayleigh velocity measured by the monitoring system from June to August 2015.

Figure 15. Comparison between (a) rainfall and cumulative displacement, (b) displacement rate and (c) Rayleigh velocity measured by the monitoring system before the reactivation of February 25, 2015.

Figure 16. Comparison between (a) rainfall and cumulative displacement, (b) displacement rate and (c) Rayleigh velocity measured by the monitoring system during the suspended phase from July to November 2014.

Figure 17. Charts showing the variation of Rayleigh velocity at a depth of 2 m (a) and the corresponding variation of small-strain shear stiffness (b) with the time elapsed after a surge. Each point represents the mean value of V_r or G_0 obtained by periodic surveys inside (gray dots) or outside (black triangles) the landslide area.

Figure 18. Variation of the normalized void ratio (see text) with the time elapsed after a surge. Each point represents the mean value of void ratio obtained by periodic surveys inside the landslide area. Red lines indicate the theoretical trend predicted by the one-dimensional Terzaghi equation for two values of the coefficient of consolidation c_v typical of fine-grained materials.

Figure 1.

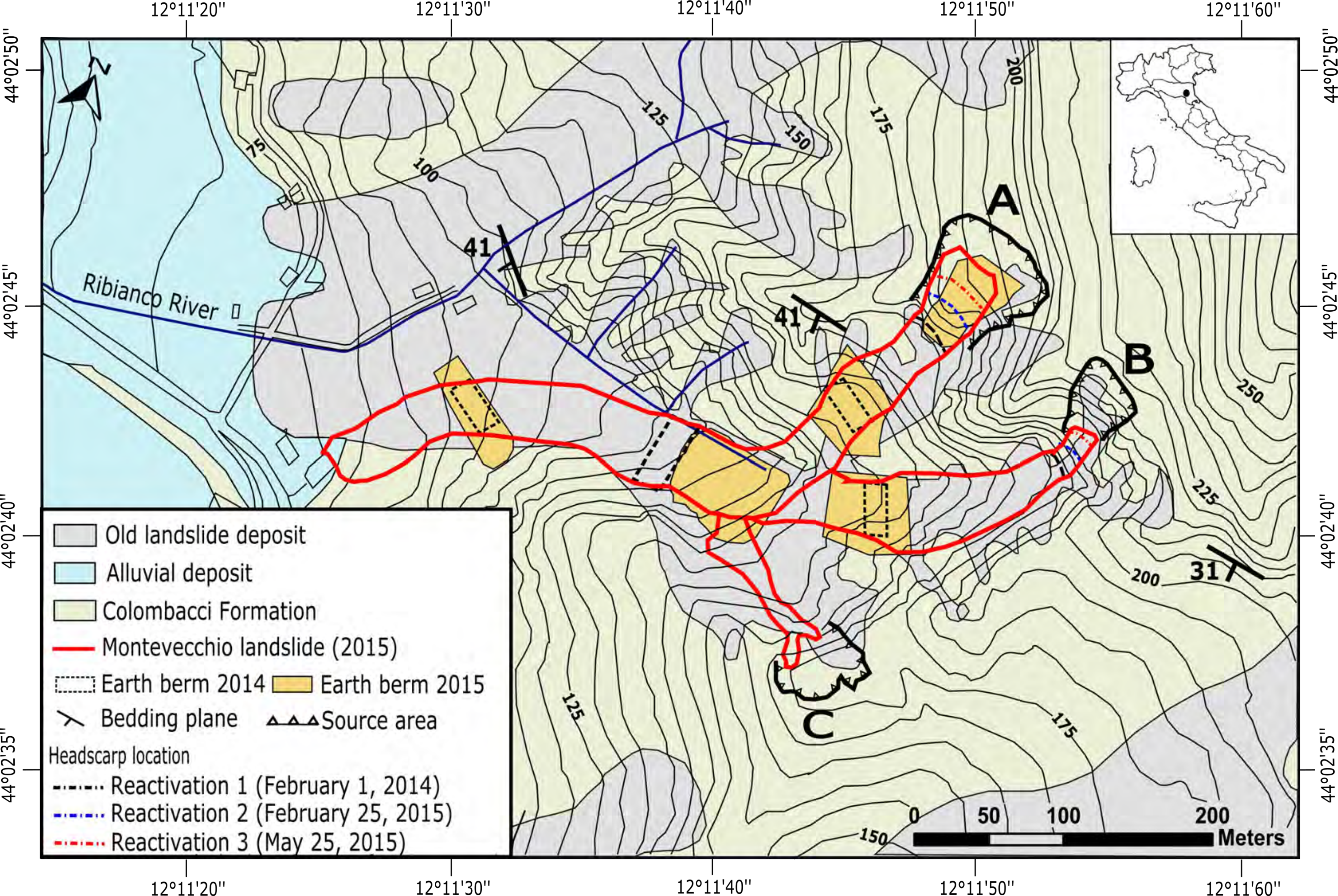

12°11'20''
12°11'30''
12°11'40''
12°11'50''
12°11'60''
44°02'50''
44°02'45''
44°02'40''
44°02'35''
N
Ribianco River
75
100
125
150
175
200
225
250
41
31
A
B
C
Old landslide deposit
Alluvial deposit
Colombacci Formation
Montevecchio landslide (2015)
Earth berm 2014
Earth berm 2015
Bedding plane
Source area
Headscarp location
Reactivation 1 (February 1, 2014)
Reactivation 2 (February 25, 2015)
Reactivation 3 (May 25, 2015)
0
50
100
200
Meters

Figure 2.


a
d
c
b
25 m
45 m
a
35 m
b
c
d

Figure 3.

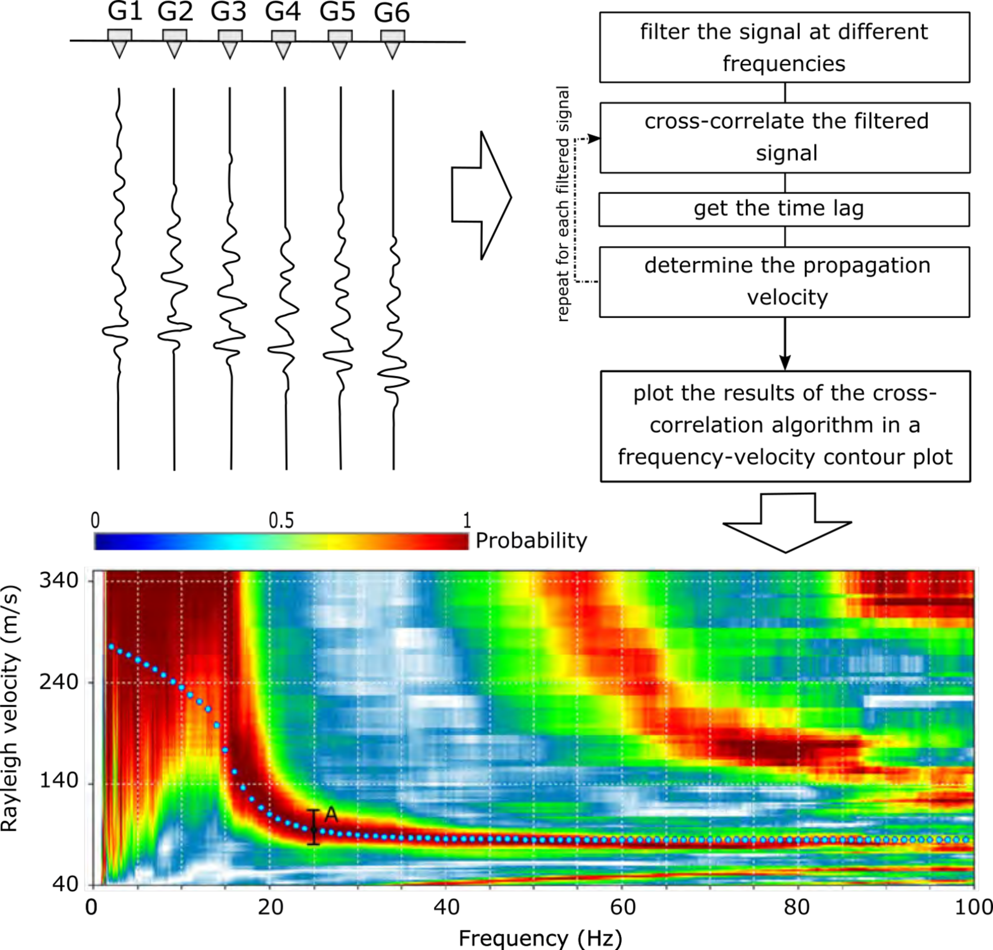
G1
G2
G3
G4
G5
G6
filter the signal at different frequencies
cross-correlate the filtered signal
get the time lag
determine the propagation velocity
repeat for each filtered signal
plot the results of the cross-correlation algorithm in a frequency-velocity contour plot
0
0.5
1
Probability
Rayleigh velocity (m/s)
340
240
140
40
A
0
20
40
60
80
100
Frequency (Hz)

Figure 4.

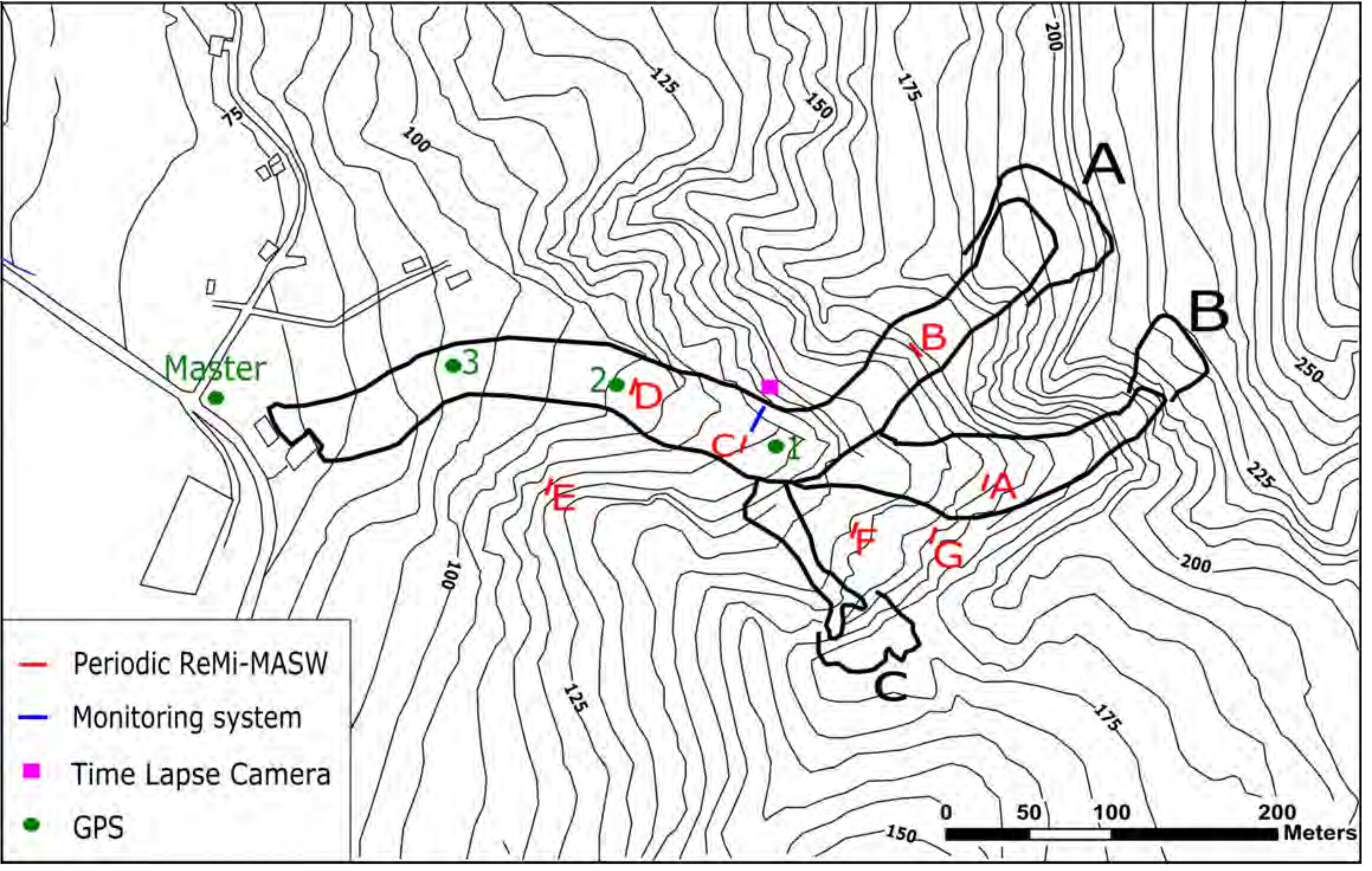
A
B
C
Master
1
2
3
A
B
C
D
E
F
G
75
100
125
150
175
200
225
250
Periodic ReMi-MASW
Monitoring system
Time Lapse Camera
GPS
0
50
100
200
Meters

Figure 5.

7 m
a
b
c

Figure 6..

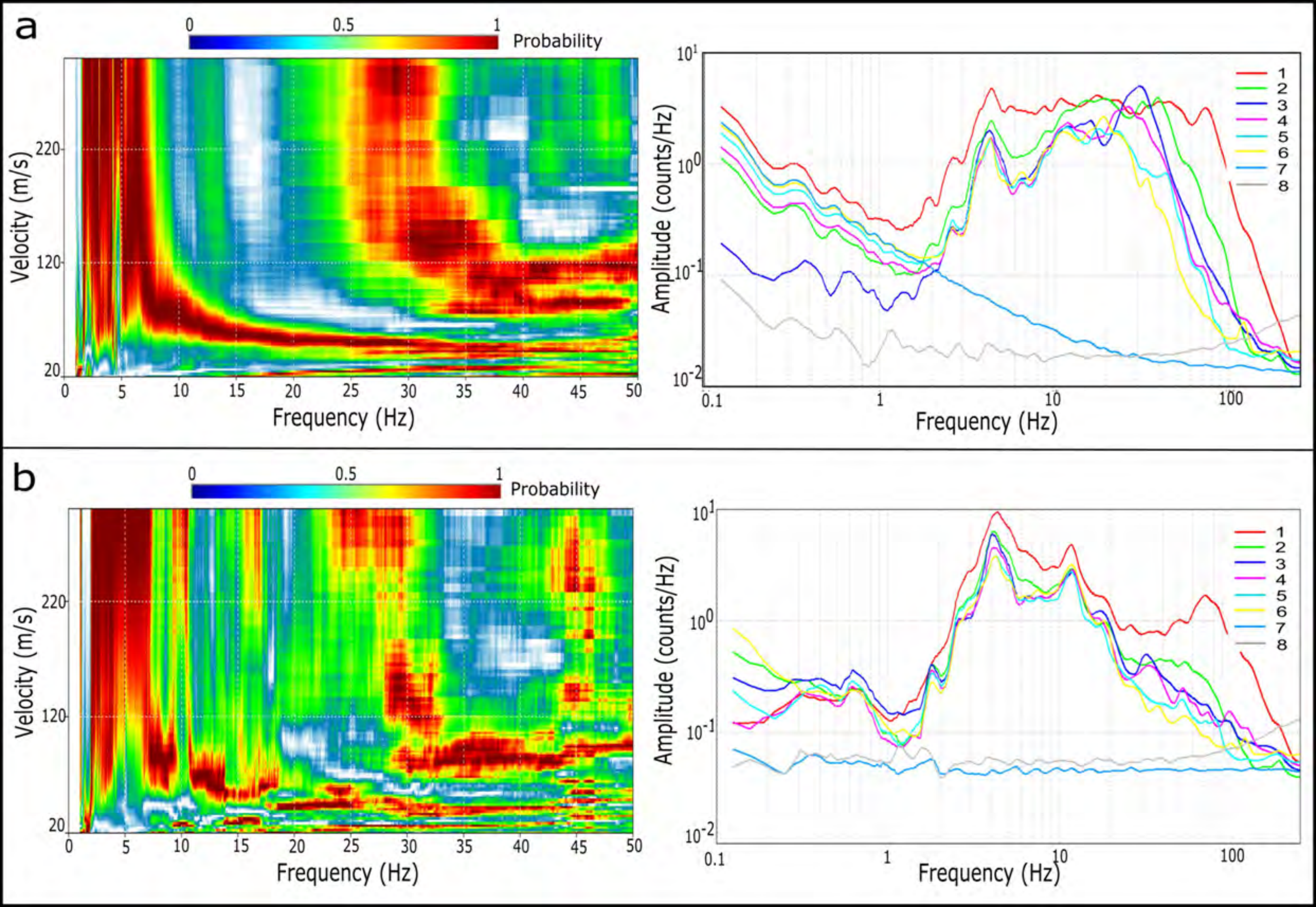

a
b
Probability
Velocity (m/s)
Frequency (Hz)
Amplitude (counts/Hz)
1
2
3
4
5
6
7
8

Figure 7.


a
b
c
d

Figure 8.

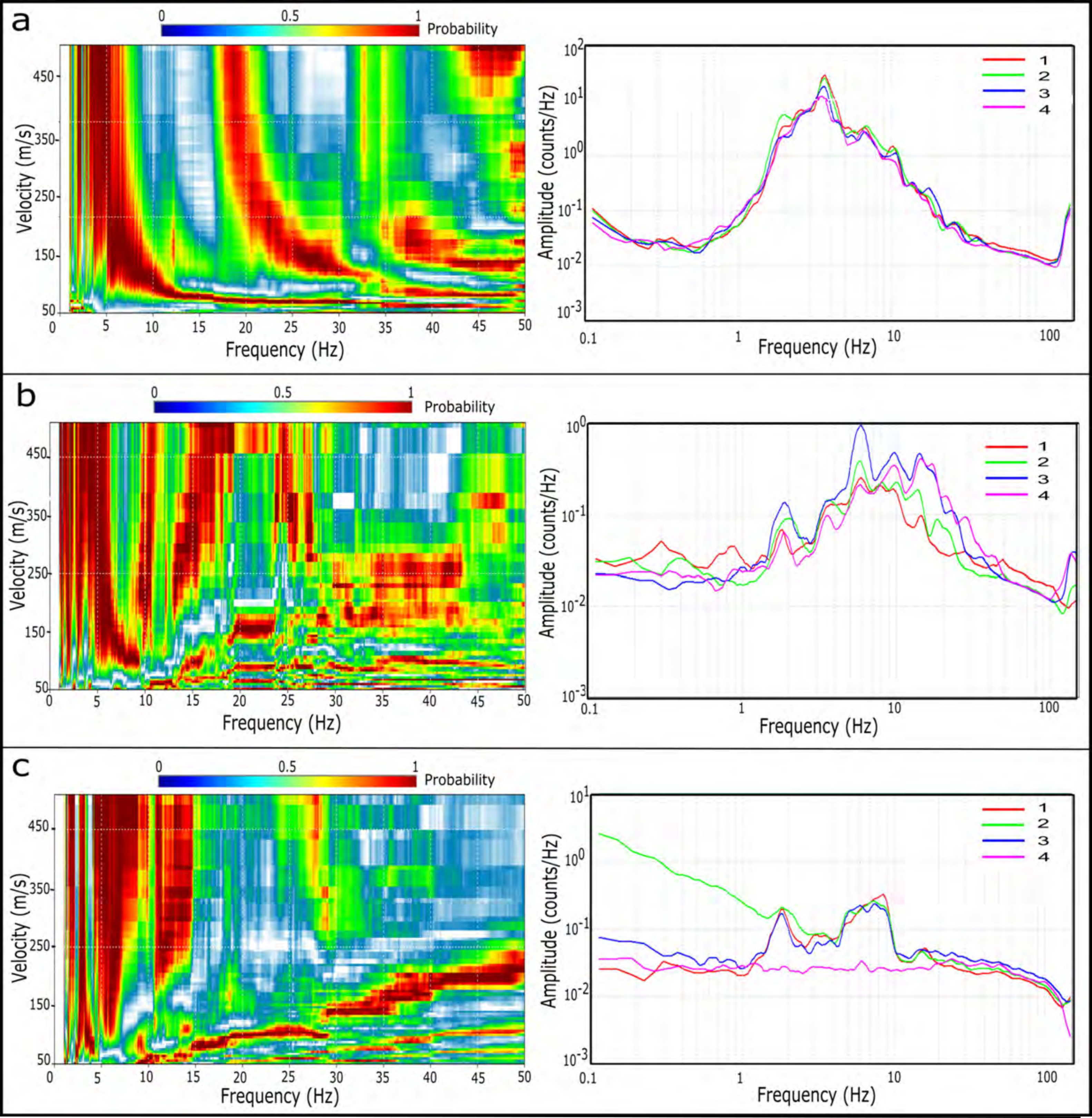

a
0
0.5
1
Probability
Velocity (m/s)
Frequency (Hz)
Amplitude (counts/Hz)
1
2
3
4
b
0
0.5
1
Probability
Velocity (m/s)
Frequency (Hz)
Amplitude (counts/Hz)
1
2
3
4
c
0
0.5
1
Probability
Velocity (m/s)
Frequency (Hz)
Amplitude (counts/Hz)
1
2
3
4

Figure 9.

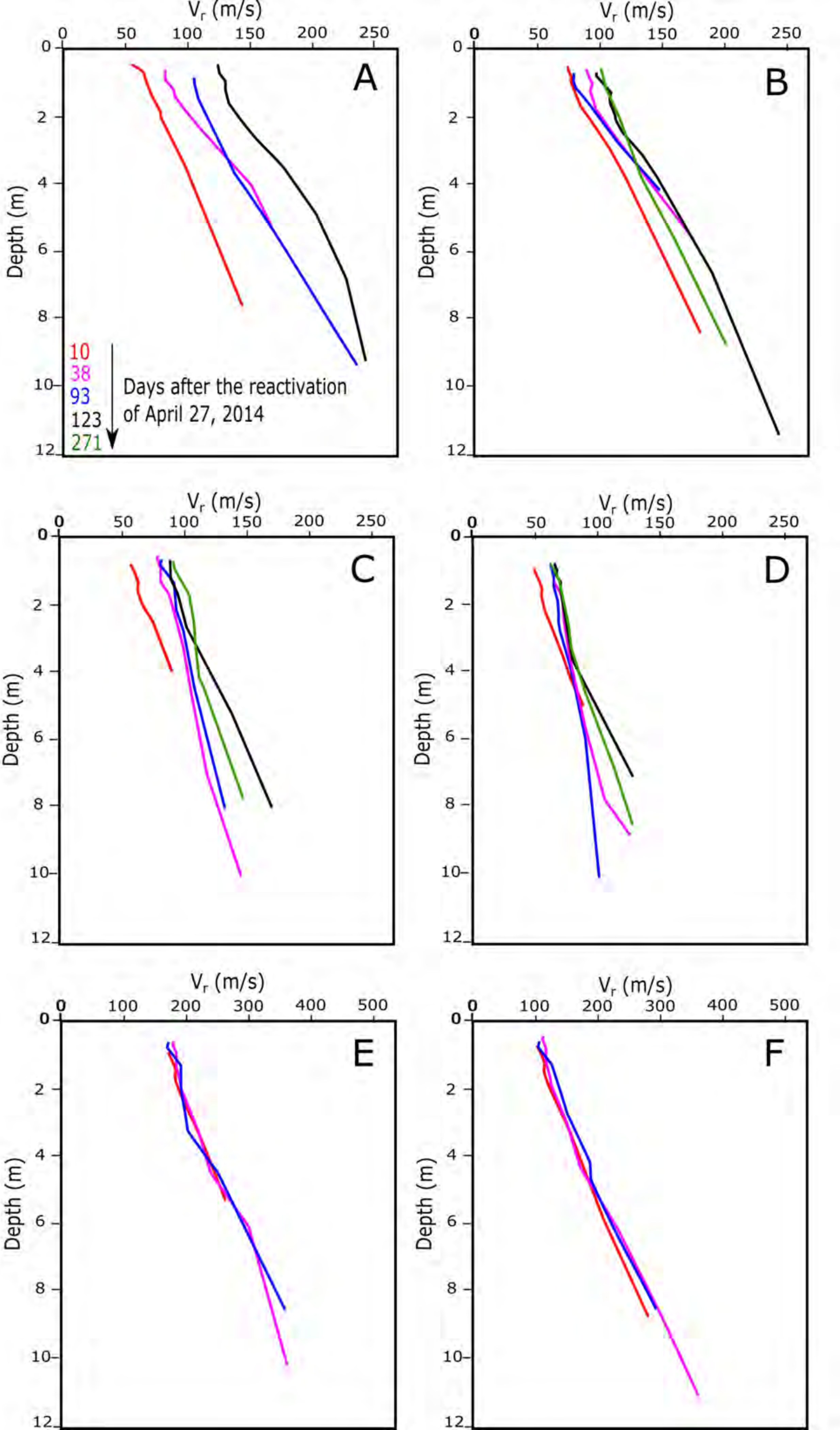

Vr (m/s)
A
B
C
D
E
F
Depth (m)
10
38
93
123
271
Days after the reactivation of April 27, 2014

Figure 10.

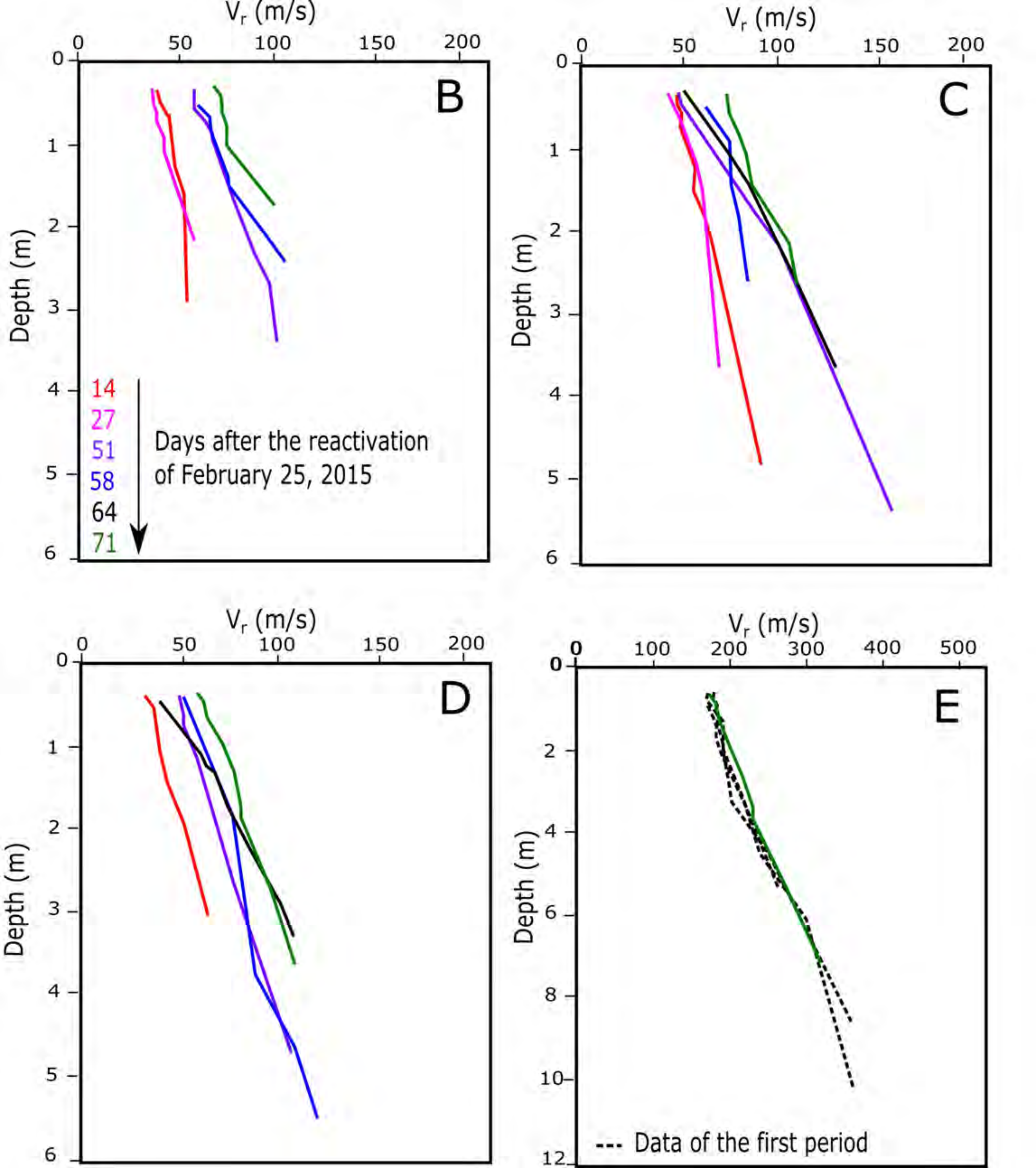

Vr (m/s)
0
50
100
150
200
Depth (m)
B
14
27
51
58
64
71
Days after the reactivation
of February 25, 2015
C
D
E
300
400
500
Data of the first period

Figure 11.

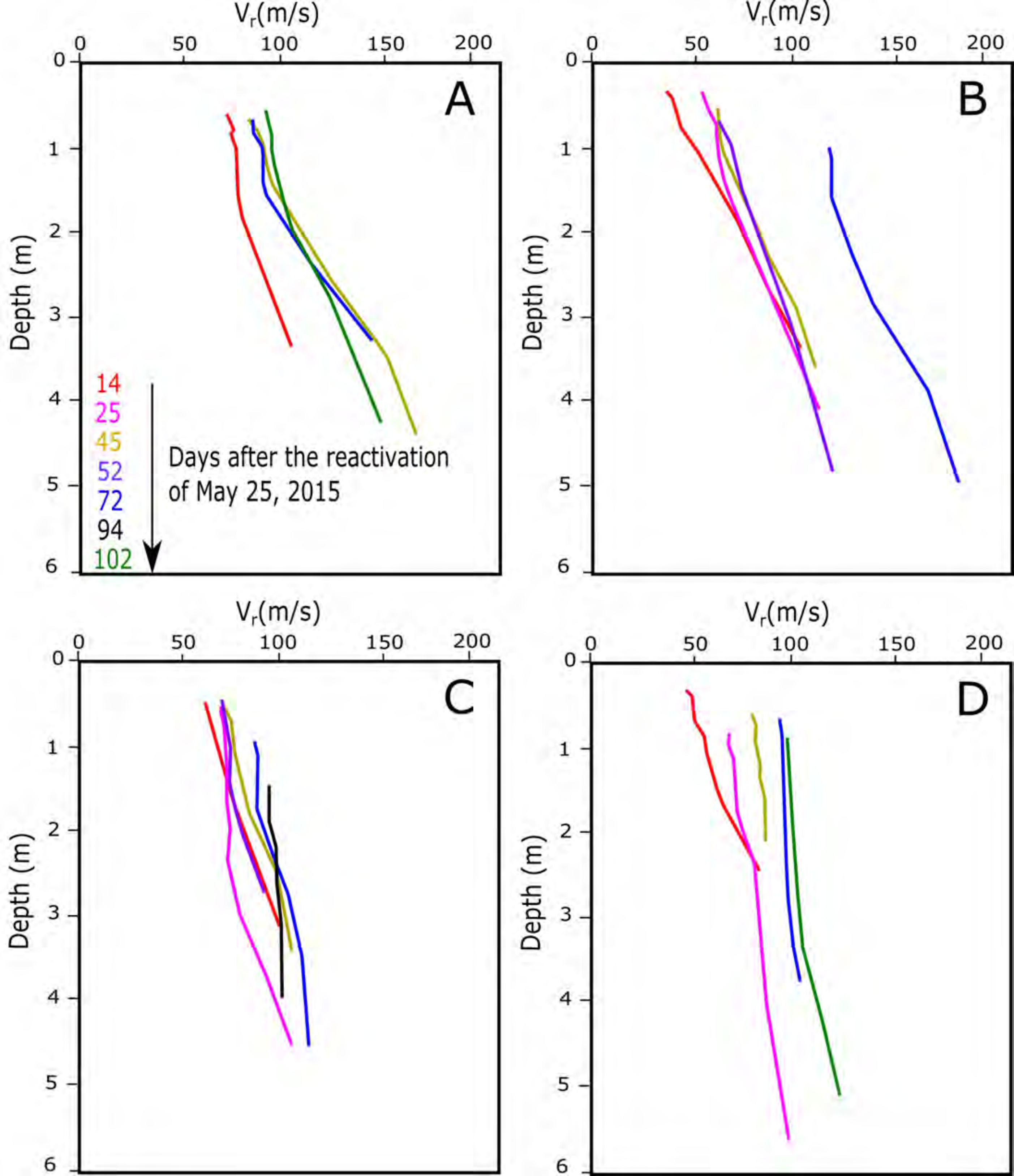

V_r(m/s)
Depth (m)
A
B
C
D
14
25
45
52
72
94
102
Days after the reactivation of May 25, 2015

Figure 12.

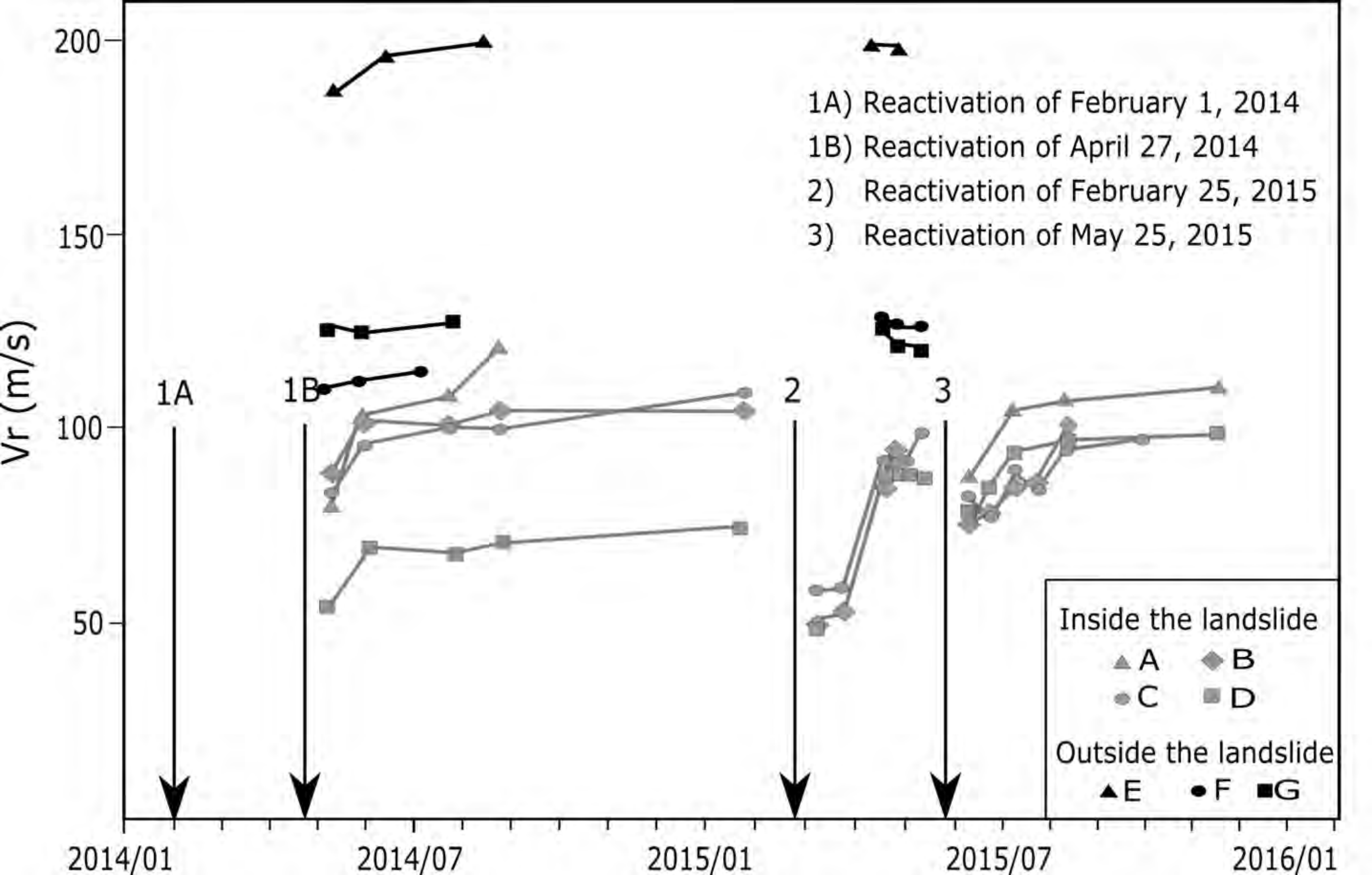

200
150
100
50
Vr (m/s)
1A) Reactivation of February 1, 2014
1B) Reactivation of April 27, 2014
2) Reactivation of February 25, 2015
3) Reactivation of May 25, 2015
1A
1B
2
3
Inside the landslide
A
B
C
D
Outside the landslide
E
F
G
2014/01
2014/07
2015/01
2015/07
2016/01

Figure 13.

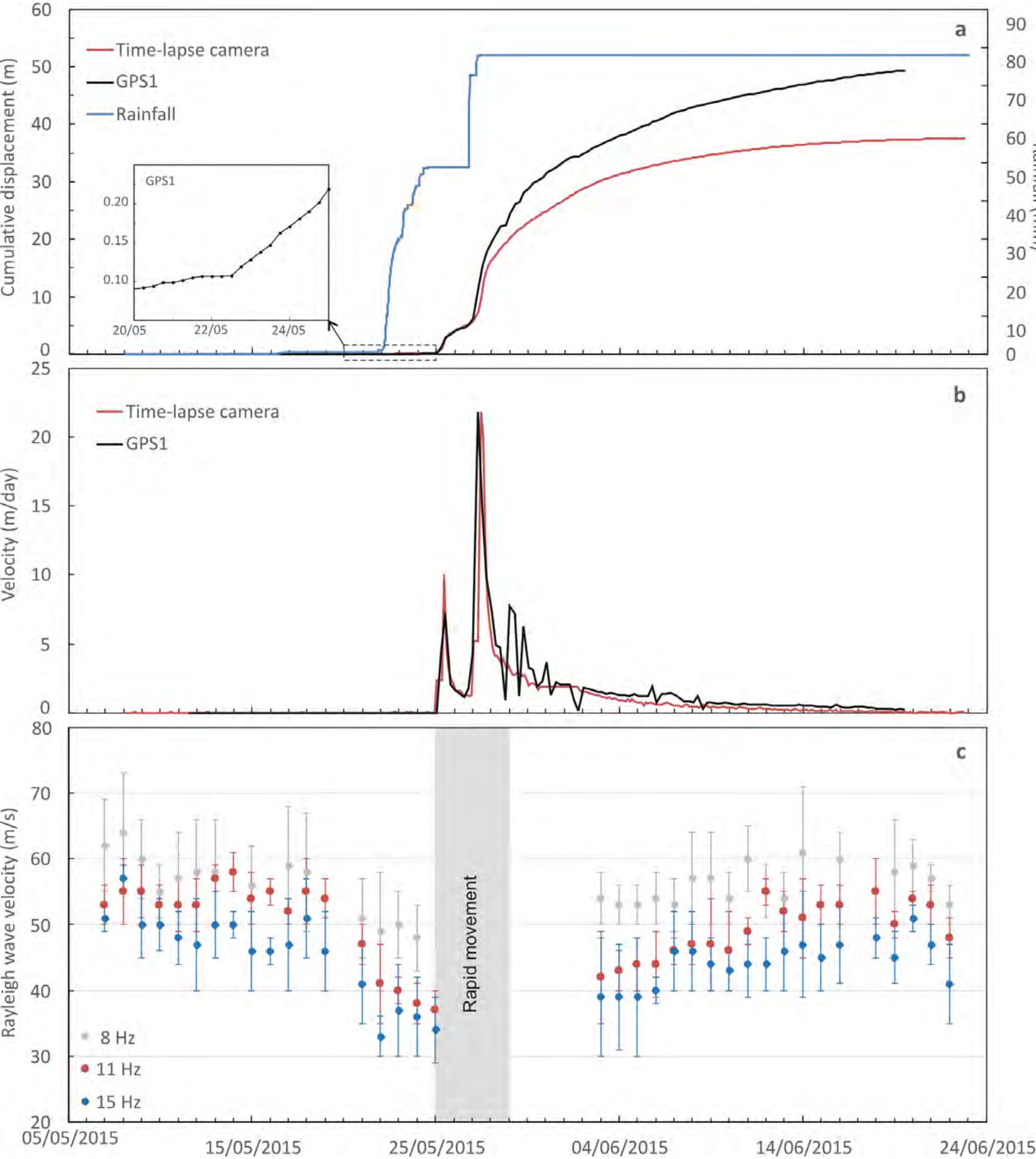

a
Time-lapse camera
GPS1
Rainfall
Cumulative displacement (m)
Rainfall (mm)
GPS1
20/05
22/05
24/05
b
Time-lapse camera
GPS1
Velocity (m/day)
c
Rapid movement
Rayleigh wave velocity (m/s)
8 Hz
11 Hz
15 Hz
05/05/2015
15/05/2015
25/05/2015
04/06/2015
14/06/2015
24/06/2015

Figure 14.

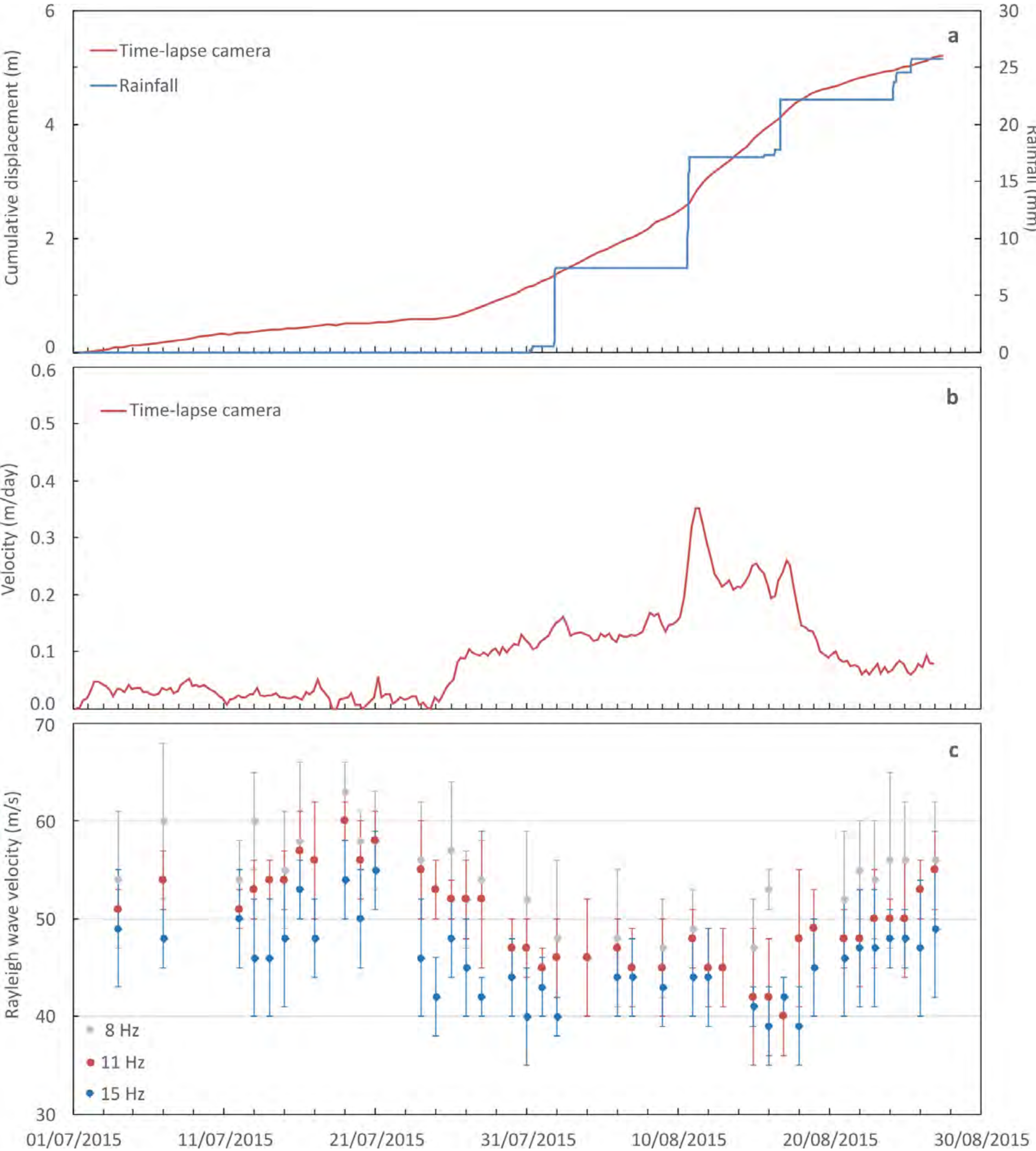
a
Time-lapse camera
Rainfall
Cumulative displacement (m)
Rainfall (mm)
b
Time-lapse camera
Velocity (m/day)
c
Rayleigh wave velocity (m/s)
8 Hz
11 Hz
15 Hz
01/07/2015
11/07/2015
21/07/2015
31/07/2015
10/08/2015
20/08/2015
30/08/2015

Figure 15.

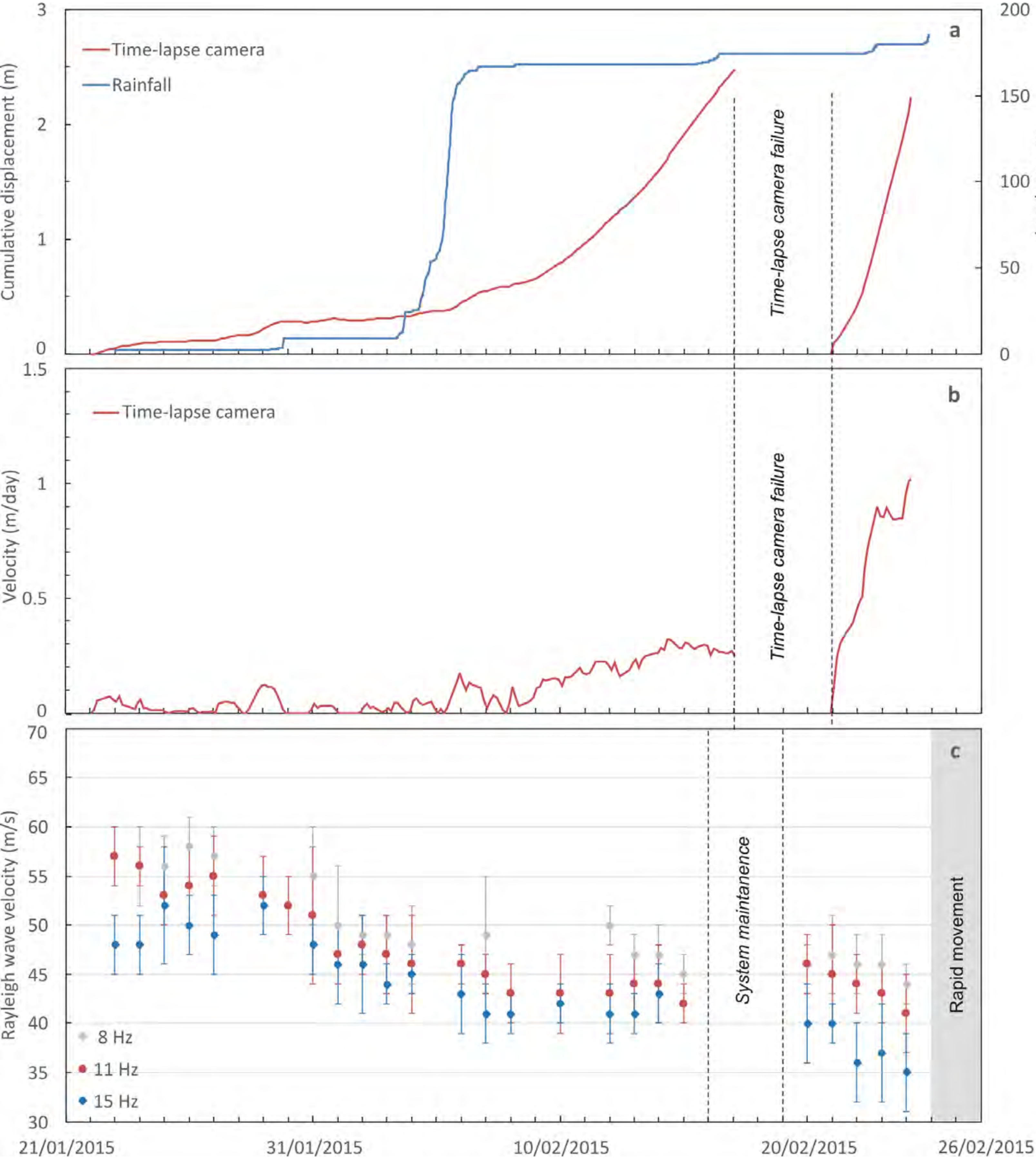

a
Time-lapse camera
Rainfall
Cumulative displacement (m)
Rainfall (mm)
Time-lapse camera failure
b
Time-lapse camera
Velocity (m/day)
Time-lapse camera failure
c
Rayleigh wave velocity (m/s)
System maintanence
Rapid movement
8 Hz
11 Hz
15 Hz
21/01/2015
31/01/2015
10/02/2015
20/02/2015
26/02/2015

Figure 16.

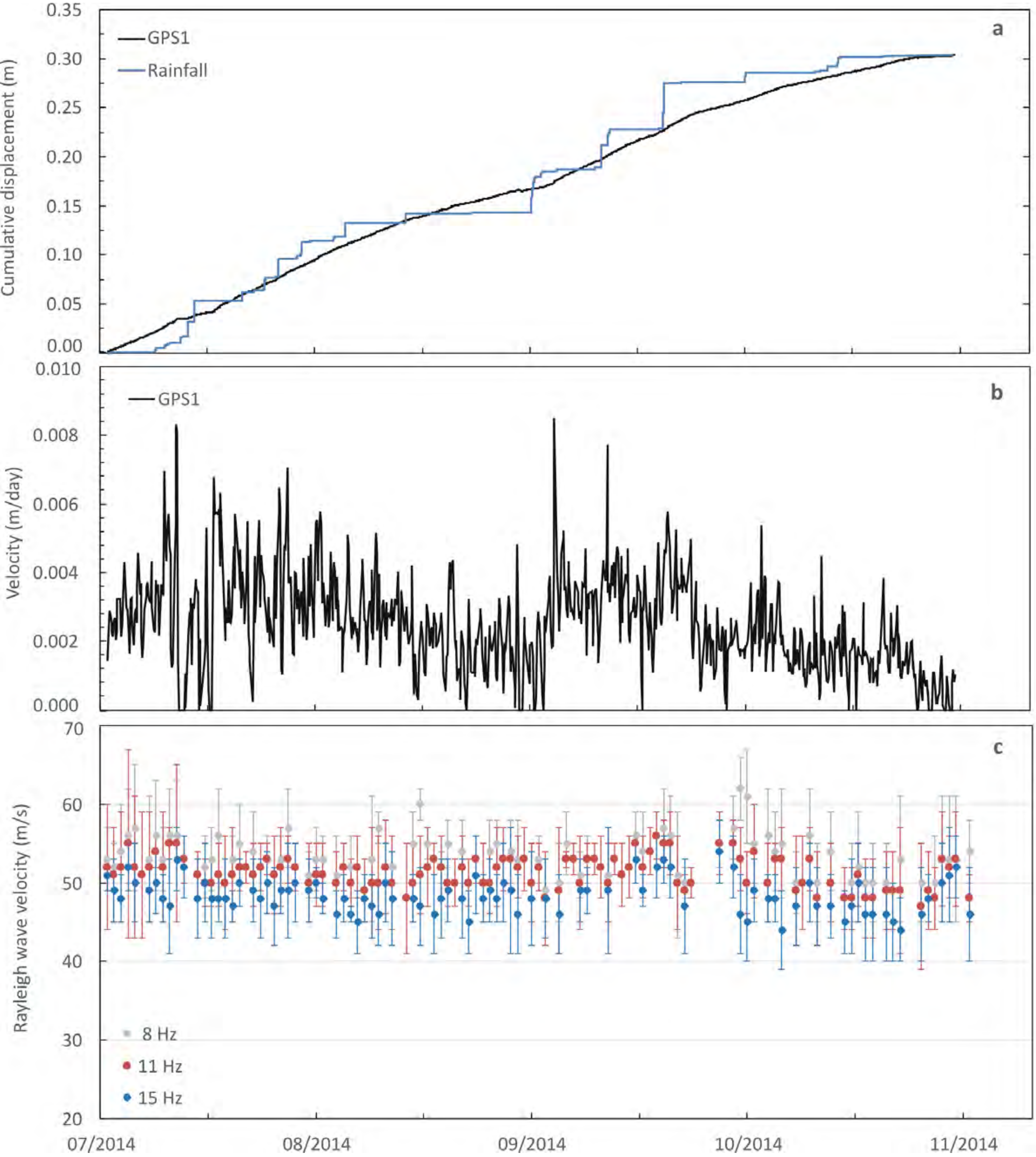

a
GPS1
Rainfall
Cumulative displacement (m)
Rainfall (mm)
0.35
0.30
0.25
0.20
0.15
0.10
0.05
0.00
350
300
250
200
150
100
50
0
b
GPS1
Velocity (m/day)
0.010
0.008
0.006
0.004
0.002
0.000
c
Rayleigh wave velocity (m/s)
70
60
50
40
30
20
8 Hz
11 Hz
15 Hz
07/2014
08/2014
09/2014
10/2014
11/2014

Figure 17.

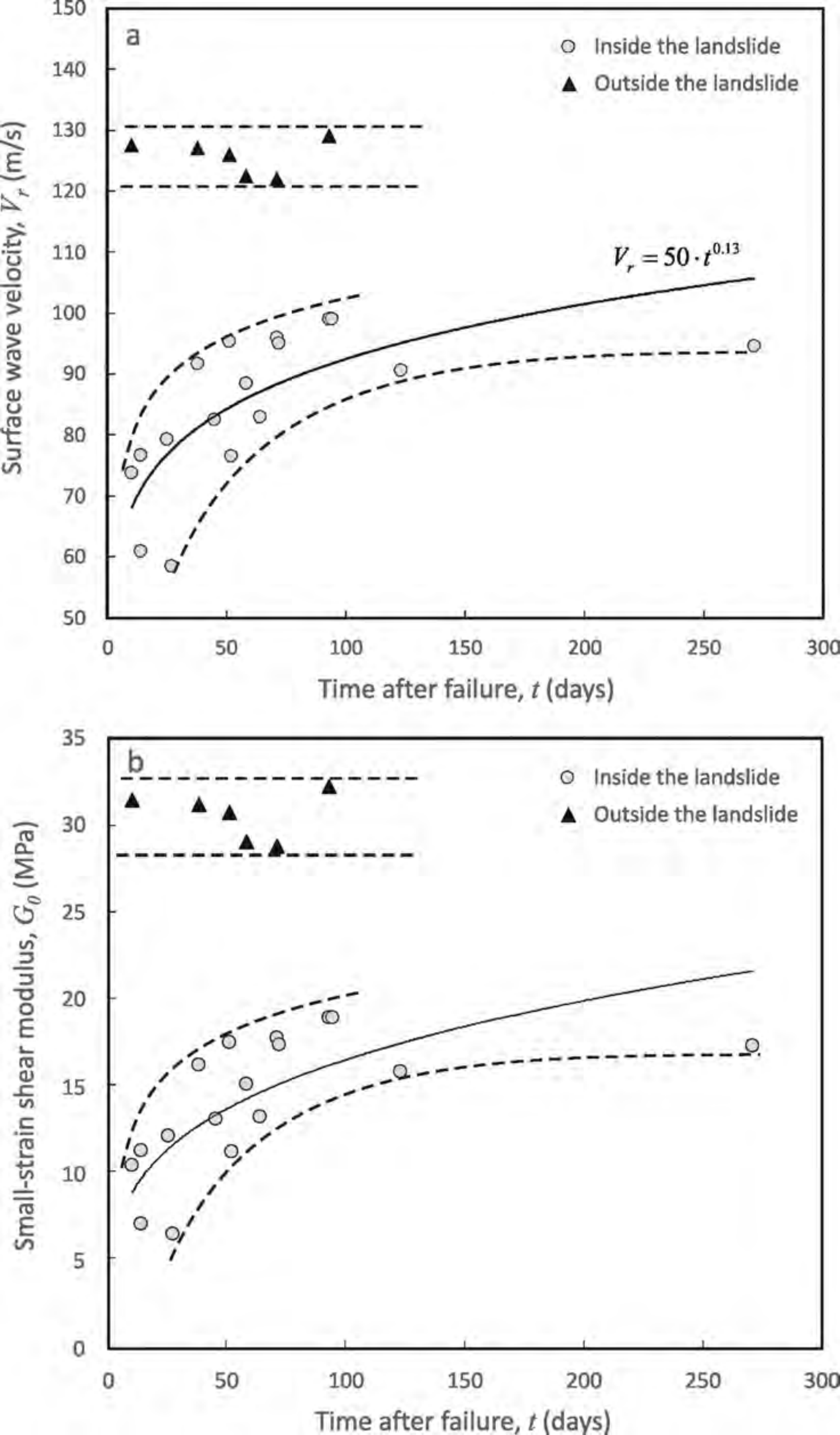

a
Inside the landslide
Outside the landslide
$V_r = 50 \cdot t^{0.13}$
Surface wave velocity, V_r (m/s)
Time after failure, t (days)
b
Inside the landslide
Outside the landslide
Small-strain shear modulus, G_0 (MPa)
Time after failure, t (days)

Figure 18.

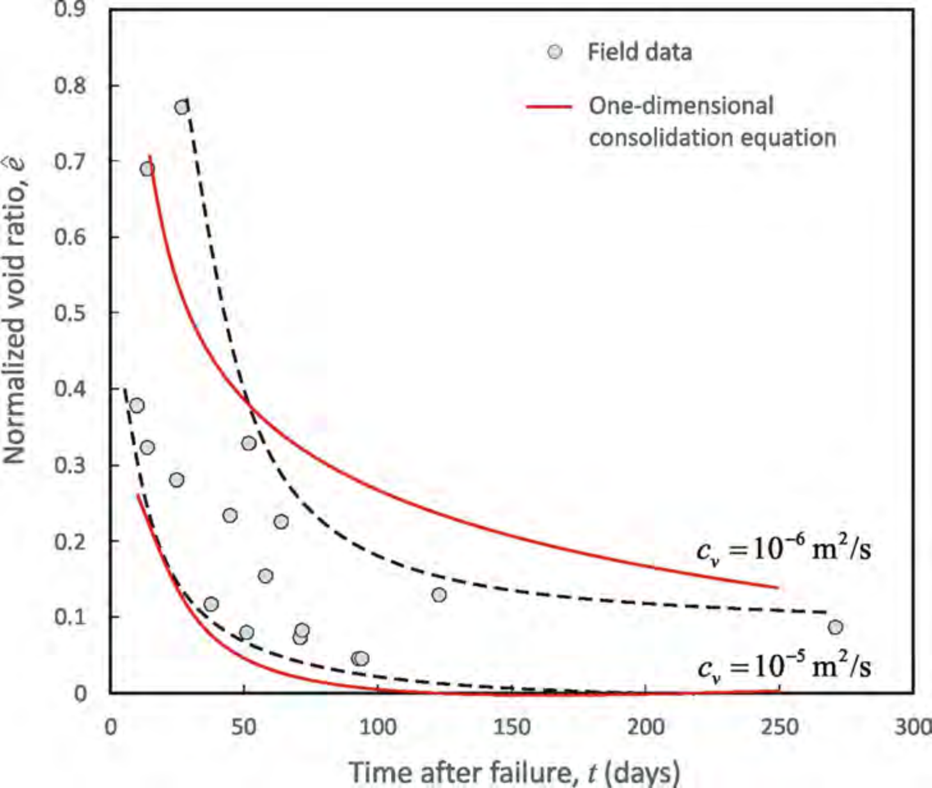

Field data
One-dimensional consolidation equation
$c_v = 10^{-6}$ m^2/s
$c_v = 10^{-5}$ m^2/s
Normalized void ratio, $\hat{e}$
Time after failure, t (days)
0
0.1
0.2
0.3
0.4
0.5
0.6
0.7
0.8
0.9
0
50
100
150
200
250
300